Key Point:
- Fault slip modes at the plate boundary in erosive subduction zones are governed by subducted sediments carried by the incoming plate

Frictional Properties of Subduction Input Sediments at an Erosive Convergent Continental Margin and Related Controls on Décollement Slip Modes: The Costa Rica Seismogenesis Project

Robert Marek Kurzawski[1,2] , André Rik Niemeijer[3] , Michael Stipp[4] , Delphine Charpentier[5], Jan Hinrich Behrmann[1], and Christopher James Spiers[3]

[1]GEOMAR Helmholtz Centre for Ozean Research Kiel, Kiel, Germany, [2]Institute of Geosciences, University of Kiel (CAU), Kiel, Germany, [3]HPT Laboratory, Utrecht University, Utrecht, Netherlands, [4]Institute of Geology, University of Innsbruck, Innsbruck, Austria, [5]Université de Franche-Comté, Besancon, France

Abstract The spectrum of slip modes occurring along shallow portions of the plate boundary décollement in subduction zones includes aseismic slip, slow slip, and seismogenic slip. The factors that control slip modes directly influence the hazard potential of subduction zones for generating large-magnitude earthquakes and tsunamis. We conducted an experimental study of the frictional behavior of subduction input sediments, recovered from two Integrated Ocean Drilling Program expeditions to the erosive subduction margin offshore Costa Rica (Expeditions 334 and 344), employing rotary shear under hydrothermal conditions. The velocity dependence of friction was explored, using simulated gouges prepared from all major lithologies, covering a wide range of conditions representative for the initial stages of subduction. Temperature, effective normal stress, and pore fluid pressure were varied systematically up to 140 °C, 110 MPa, and 120 MPa, respectively. Sliding velocities up to 100 μm/s, relevant for earthquake rupture nucleation and slow slip, were investigated. The only sediment type that produced frictional instabilities (i.e., laboratory earthquakes) was the calcareous ooze carried by the incoming Cocos Plate, which by virtue of its slip-weakening behavior is also a likely candidate for triggering slow slip events. We evaluate this mechanism of producing unstable slip and consider alternatives. Therefore, locking and unlocking of plate boundary megathrusts are not only related to variations in pore fluid pressure but may also depend on the presence of pelagic carbonate-rich lithologies. Subduction systems containing such input are likely low latitude, where extensive deposition of carbonates takes place above the carbonate compensation depth.

1. Introduction

Deformation processes related to the plate boundary interface in subduction zones, also termed the décollement or megathrust, comprise a wide spectrum of tectonic fault slip modes including slow slip events (SSEs) and regular megathrust earthquakes, which are the most destructive natural disasters on planet Earth. Related ruptures are several hundreds of kilometers long, potentially tearing apart entire segments of major subduction zones and causing devastating tsunamis. In fault mechanics, the rupture area provides a first-order estimate of the energy release of a related earthquake and therefore its magnitude. Knowledge of the extent of the seismogenic zone of subduction megathrust faults is therefore fundamental for hazard assessment, as it constrains (1) the size of the maximum rupture area and (2) the potential for exceptionally shallow seismogenesis causing a high risk for tsunami earthquakes.

The nucleation of large plate boundary earthquakes is limited to depths between ≈10 and 40 km at most active continental margins (Byrne et al., 1988; Hyndman & Wang, 1993; Shimamoto et al., 1993). Parameters and processes controlling especially the updip limit of this so-called seismogenic zone are not satisfactorily characterized to date and remain a matter of debate. The classical model assigns a major role to the dehydration of clay minerals and especially the thermally controlled transition from smectite to illite clays, which in most cases happens to coincide with the onset of seismicity within the temperature range between 120 and 150 °C (Hyndman et al., 1997; Oleskevich et al., 1999; Pytte & Reynolds, 1989; Saffer & Marone, 2003).

Increasing pore fluid pressure causes the overall stress state to converge to its critical point of failure where hydrofracturing is triggered by reduction of effective normal stress (Clayton et al., 1995; Terzaghi, 1923), an important expansion of the Mohr-Coulomb theory (Coulomb, 1776; Mohr, 1900). If trapped within, or hindered from escaping by overlying low permeability materials, original pore water is pressurized by sediment compaction and diagenesis within the first $\approx 3 - 7$ km of burial (Bekins & Dreiss, 1992; Bray & Karig, 1985; Saffer & Tobin, 2011). Pore space reduction and additional fluid supply from mineral dehydration reactions are thought to generate the required overpressure favoring rupture nucleation.

Hydrous smectite clays are frictionally weak with friction coefficients in the range of $\mu \approx 0.1 - 0.3$ (e.g., Logan & Rauenzahn, 1987; Lupini et al., 1981; Morrow et al., 1992; Saffer et al., 2001, 2012), whereas anhydrous illite clays are frictionally stronger with $\mu \approx 0.35 - 0.49$ (e.g., Mitchell & Soga, 2005; Morrow et al., 2000, 1992, 1982). The transition from smectite to illite therefore not only adds volatiles to the system but also leads to bulk strengthening of subduction channel sediments, thereby increasing the potential for elastic stress buildup and ultimate release in a seismic event. The nucleation of seismic ruptures, however, is not governed by the absolute frictional strength but rather by the frictional stability of the host material. In particular, it requires velocity-weakening and frictionally unstable behavior (Marone, 1998a; Scholz, 1998). In contrast to the widely expected potentially unstable velocity-weakening behavior, illite shale consistently shows only velocity-strengthening behavior in friction experiments (Saffer & Marone, 2003). It is therefore unlikely that the transition from smectite to illite is the dominant mechanism controlling the onset of shallow seismogenesis.

Recently, carbonates gained increasing attention in natural and experimental deformation studies on earthquake nucleation. Numerous field-based (e.g., Carpenter et al., 2014; Tesei et al., 2013) and experimental studies (e.g., Chen et al., 2015; Ikari, Niemeijer, et al., 2013; Kurzawski et al., 2016; Spagnuolo et al., 2015; Tesei et al., 2014; Vannucchi et al., 2017; Verberne et al., 2013; Verberne, Plümper, et al., 2014; Verberne, Spiers, et al., 2014) report on microstructural and mechanical properties of carbonates, which may influence seismogenesis significantly in various tectonic settings and especially at or close to the updip limit of the seismogenic zone within subduction channels.

Here we present results of rotary shear friction experiments conducted on simulated fault gouges prepared from various natural subduction input sediments with variable clay and carbonate content. The sediments were recovered offshore Costa Rica in the course of the Expeditions 334 and 344 of the Integrated Ocean Drilling Program (IODP). This so-called Costa Rica Seismogenesis Project (CRISP) is the first drilling program aimed at investigating the genesis of large earthquakes and related tsunamis at an erosive active continental margin. Due to the erosive character of the subduction zone beneath Costa Rica, all materials from both the incoming oceanic plate and the overriding continental plate may be transported into the subduction channel. The frictional properties of these sediments will control deformation and seismogenesis within the subduction channel and along the plate boundary.

The aim of this study is a comprehensive characterization of the mechanical properties of all major lithologies might be important for deformation at the updip limit of seismogenesis at an erosive continental margin and are accessible by scientific drilling. The mechanical behavior is expected to change with increasing temperature and pressure conditions during progressive subduction. We therefore picked nine representative samples from four different CRISP drill sites covering all major lithologies and experimentally deformed them over a wide range of conditions characteristic of the shallow portions ($\approx 0 - 12$ km) of subduction megathrust faults at erosive margins.

2. Study Area

At the Middle America Trench (MAT) in the eastern Pacific Ocean oceanic lithosphere of the Cocos Plate is underthrusting the continental Carribean Plate toward the northeast at a convergence rate of 70 to 90 mm/a (DeMets, 2001; Protti et al., 1995, 1994; Figure 1). Cocos Plate lithosphere was formed at two different spreading centers, the fast spreading East Pacific Rise and the slow spreading Cocos-Nazca spreading center, and therefore features significant lateral changes in heat flow and relief, causing a distinct shift in seismicity to shallower levels where Cocos-Nazca spreading center crust is subducted (Barckhausen et al., 2001; von Huene et al., 2000; Ranero & von Huene, 2000; Vannucchi et al., 2003, 2001). Off Costa Rica and Panama, the Cocos Ridge is subducted as part of the incoming plate (Walther, 2003), significantly influencing the subduction system as explained in the following.
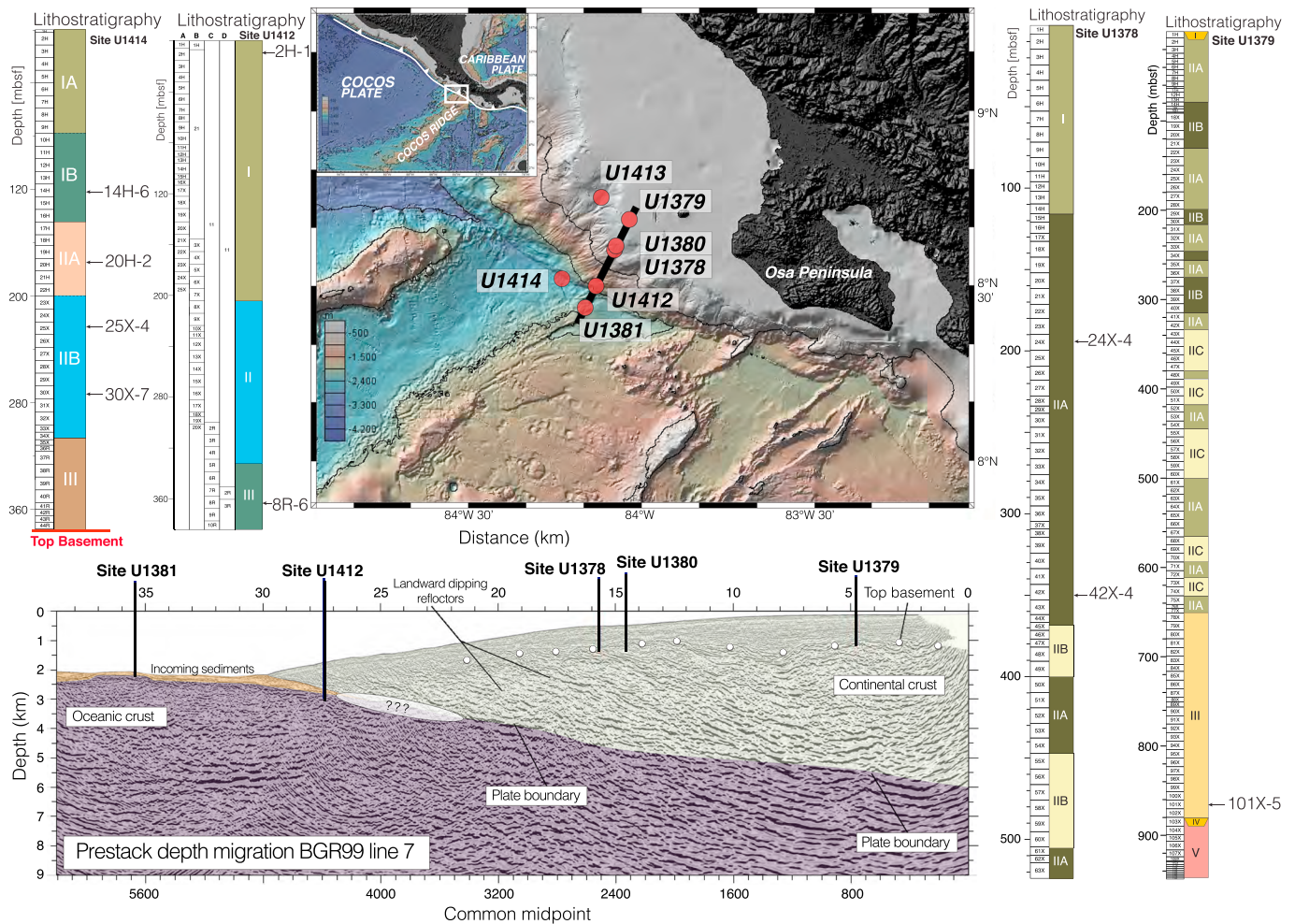
Figure 1. Map, seismic section, and lithostratigraphic columns of drilling sites at the CRISP area offshore Costa Rica. Large bathymetric map showing the surface expression of the plate boundary system offshore Osa Peninsula and tectonic overview inset map were compiled using the online map repository GeoMapApp (geomapapp.org). Location of the seismic line *BGR99-line 7* is indicated by thick black line; red dots and labels represent CRISP drilling sites. Water depths are indicated by color scale. Stratigraphic positions of samples used for mechanical tests are indicated by arrows next to lithostratigraphic columns. Lithostratigraphic units are described in the main text. CRISP = Costa Rica Seismogenesis Project.

The area is one of the best studied convergent plate boundaries on the planet and is a case example of an erosive active continental margin. It was recently found that the Costa Rica forearc is a depositional forearc, which is a special case for erosive subduction margins (Vannucchi et al., 2016). Here extreme subduction erosion causes rapid upper plate subsidence and a coeval formation of a forearc basin, which is simultaneously filled by continental slope sediments (Vannucchi et al., 2016). This self-sustained mode of forearc development implies that even at high sedimentation rates, the slope sediments are deposited before reaching the trench.

Subduction erosion occurs along the entire MAT (Clift & Vannucchi, 2004; Ranero et al., 2000; Ranero & von Huene, 2000) and is intensified due to the collision of the Cocos Ridge offshore Osa Peninsula since its onset in the Gelasian (≈2.2 Ma; Vannucchi et al., 2013, 2016). The Cocos Ridge, an aseismic magmatic ridge related to Galapagos hot spot magmatism, forms an up to 2.5-km-high subaqueous mountain chain with respect to the surrounding ocean floor (Walther, 2003). It represents a rigid indenter (LaFemina et al., 2009) that impinges the forearc wedge of the overriding plate in an approximately perpendicular orientation and parallel to the convergence direction (Figure 1). Cocos Ridge subduction induces a steepening of the geothermal gradient (Ranero et al., 2008) and results in a shift in seismicity toward a much shallower level as specified in the following paragraph.

The well-known seismic record along the MAT includes historic earthquakes of magnitude $M_w > 7$ and tsunamigenic earthquakes. It was used to characterize the geometry of the plate boundary interface and the extent of the seismogenic zone and to link seismicity patterns to the relief of the downgoing plate in numerous studies (Arroyo et al., 2014; Bilek et al., 2003; DeShon et al., 2003; Husen et al., 2002; Newman et al., 2002; Protti et al., 1995). DeShon et al. (2003) determined a slab dip of 19° from an aftershock sequence that followed the 1999 M_w 6.4 Quepos event and delineated the megathrust. The same data set yielded updip and downdip seismicity limits at depths of ≈10 and 30 km. However, this applies to one seismic megathrust event, and especially heterogeneous architecture oft he downgoing Cocos plate may constrain significant differences in plate bending radii and, thus, local slab geometry (Arroyo et al., 2014, 2011; Dinc et al., 2010; Lücke & Arroyo, 2015).

Slow slip processes occur on both the deep and the shallow portions of the subduction megathrust showing maximum magnitudes equivalent to $M_w \approx 7$, and commonly, these events last a few to several weeks (e.g., Dixon et al., 2014; Jiang et al., 2012; Saffer & Wallace, 2015). In Costa Rica, the depth ranges of large earthquake ruptures and SSEs are actually overlapping in space (Jiang et al., 2012; Saffer & Wallace, 2015), allowing for an investigation of the mechanical preconditions, which may favor one, or the other mode of failure.

The CRISP study area is located on the NW flank of the Cocos Ridge (Figure 1). It comprises seven drilling sites in five different tectonic positions. Two sites on the incoming plate (U1381 and U1414) cover the entire incoming sediment succession consisting of pelagic and hemipelagic sediments and the underlying Cocos Ridge basalt. Drilling at Site U1412 revealed the accretionary character of the frontal prism, as a repeating sequence of strata comparable to those from the incoming plate was encountered implying thrust faulting (Harris et al., 2013b; Vannucchi et al., 2016, 2017). Two sites on the midslope (U1378 and U1380) characterize fine-grained clastic slope sediments, and the remaining two upper slope sites (U1379 and U1413) comprise more proximal medium to fine-grained clastic sediments including abundant sand layers. Five sites (U1381, U1412, U1378, U1380, and U1379) are situated along the seismic line BGR99-7, and the remaining two (U1414 and U1413) within a 3-D seismic survey area (Bangs et al., 2015, 2016).

3. Methods

3.1. Experimental Apparatus

Friction experiments were conducted in the unique hydrothermal rotary shear apparatus, designed and constructed at the High Pressure and Temperature Laboratory in Utrecht, the Netherlands (Niemeijer et al., 2008, Figure 2). The machine is routinely employed to study various aspects of fault mechanics, including frictional behavior and related microstructure evolution in natural and synthetic fault rocks and gouges. Due to its extraordinarily broad range of operating conditions, namely, temperatures up to $T = 700\,°C$, effective normal stress up to $\sigma_n^{\mathrm{eff}} = 300$ MPa, pore fluid pressures up to $P_f = 300$ MPa, and ultrahigh shear strains up to $\gamma \approx 100$, it is especially suitable to address progressing deformation inside subduction channels. The sample, usually a simulated fault gouge, is placed between two René 41 Superalloy pistons and laterally confined by two superalloy rings coated with MoS_2 lubricant spray (Molycote) to avoid wall friction (Figures 2b and 2c).

The sample-piston assembly is immersed in distilled water acting as pore fluid inside a pressure vessel, which is then mounted into an Instron 1362 loading frame that externally applies normal stress via a pressure-compensated loading piston. Shear stress is generated on the sample by rotating the pressure vessel together with the internally fixed lower piston via a servo-controlled motor, while the upper piston is held stationary. For detailed descriptions the reader is referred to Niemeijer et al. (2008), Den Hartog, Niemeijer, and Spiers (2012), and Den Hartog, Peach, et al. (2012).

3.2. Friction Experiments
3.2.1. Sample Preparation

In order to prepare simulated fault gouges, IODP core samples were dried at $T = 55\,°C$ for 24 hr to avoid illitization of smectite clays. Careful disaggregation of the dried material was carried out using mortar and pestle and the grain size fraction <125 μm was extracted from the disaggregated powder by sieving. The extracted material (≈0.54 g) was evenly distributed between the confining rings and the two opposing internal pistons resulting in an initial gouge layer thickness of approximately 2 mm (Figure 2c).

3.2.2. Choice of Experimental Conditions

Experimental conditions were defined to cover a wide range of conditions representative for shallow prograde subduction input trajectories, from the initial stages of subduction close to the ocean floor down to
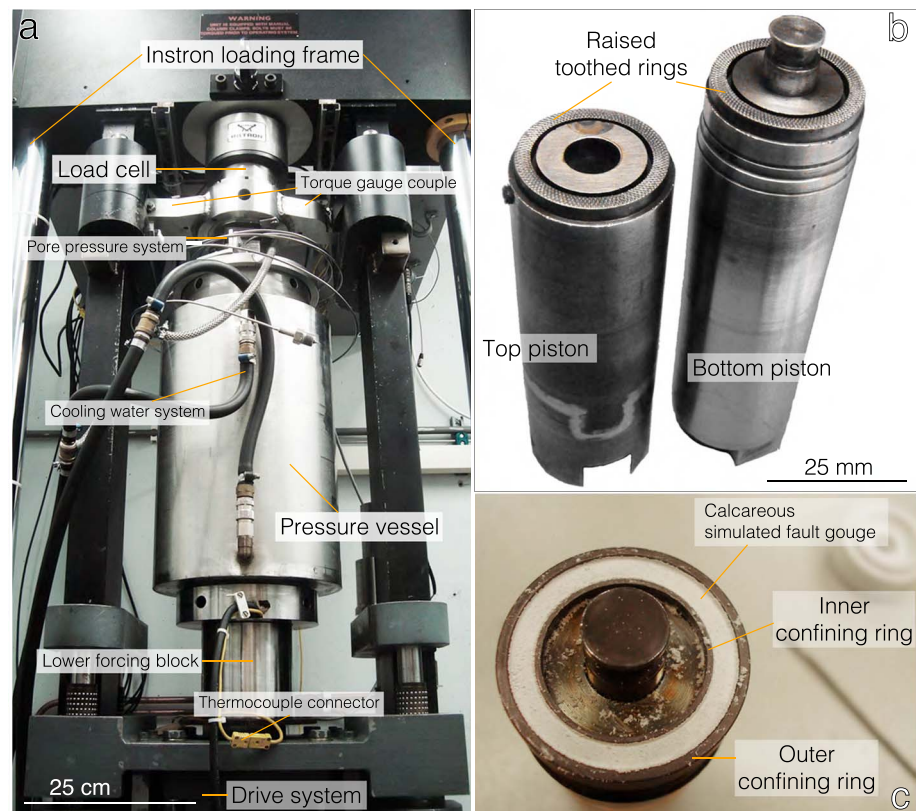
Figure 2. Photographs of experimental apparatus used in this study. (a) Hydrothermal pressure vessel mounted into Instron loading frame with important mechanical components labeled. (b) Disassembled two opposing internal pistons with exposed toothed sample contact area. (c) Lower internal piston with sample confining rings and prepared simulated fault gouge infill.

hypocentral depths, notably corresponding to the expected conditions of the updip limit of seismogenesis at approximately 5- to 6-km depth (Arroyo et al., 2014). The exact ambient conditions during progressing subduction depend on many factors, such as the local geothermal gradient and the evolution of pore fluid pressure. In subduction zones, the local thermal gradient is controlled by the age of the incoming oceanic lithosphere, its actual composition, and the thickness of the sedimentary cover sequence and also by frictional heating and fluid flow within the incoming plate (Kameda et al., 2015). The pore fluid pressure and its evolution in time and space are difficult to predict. Porosity and permeability of input sediments undergo significant changes during progressive subduction related to compaction and diagenesis. A general assumption for the shallow portions of subduction channels is that the pore fluid pressure ranges between hydrostatic and lithostatic values, owing to the fact that the sediments are water saturated while entering the trench. However, the occurrence of pore pressure transients and patches of trapped and overpressured fluids due to decreasing permeability are common (Neuzil, 1995; Saffer & Bekins, 2006; Saffer & Tobin, 2011; Spinelli et al., 2006). Moreover, variations in the geothermal gradient imply that significant changes in the stress field specific thermal domains are exposed to, as they are shifted toward greater or lower burial depths. Hence, the ambient conditions for the input materials during progressive subduction are quite variable and can differ substantially even within one single subduction zone. Facing such a large conditional variability, experimental conditions were chosen such that they closely match the expected pressure-temperature conditions of the Costa Rica subduction channel, whereas pore pressure and, of course, also slip rate, were varied in the expected limits (Tables S1 and S2 in the supporting information).

3.2.3. Testing Procedure

A consistent testing procedure was used for all experiments as illustrated in Figure 3 for experiment 42 × 47,060. During testing phase one, the desired experimental conditions were established and the system was left to equilibrate for at least 45 min in the case of heated experiments. Temperature (*T*) and pore fluid
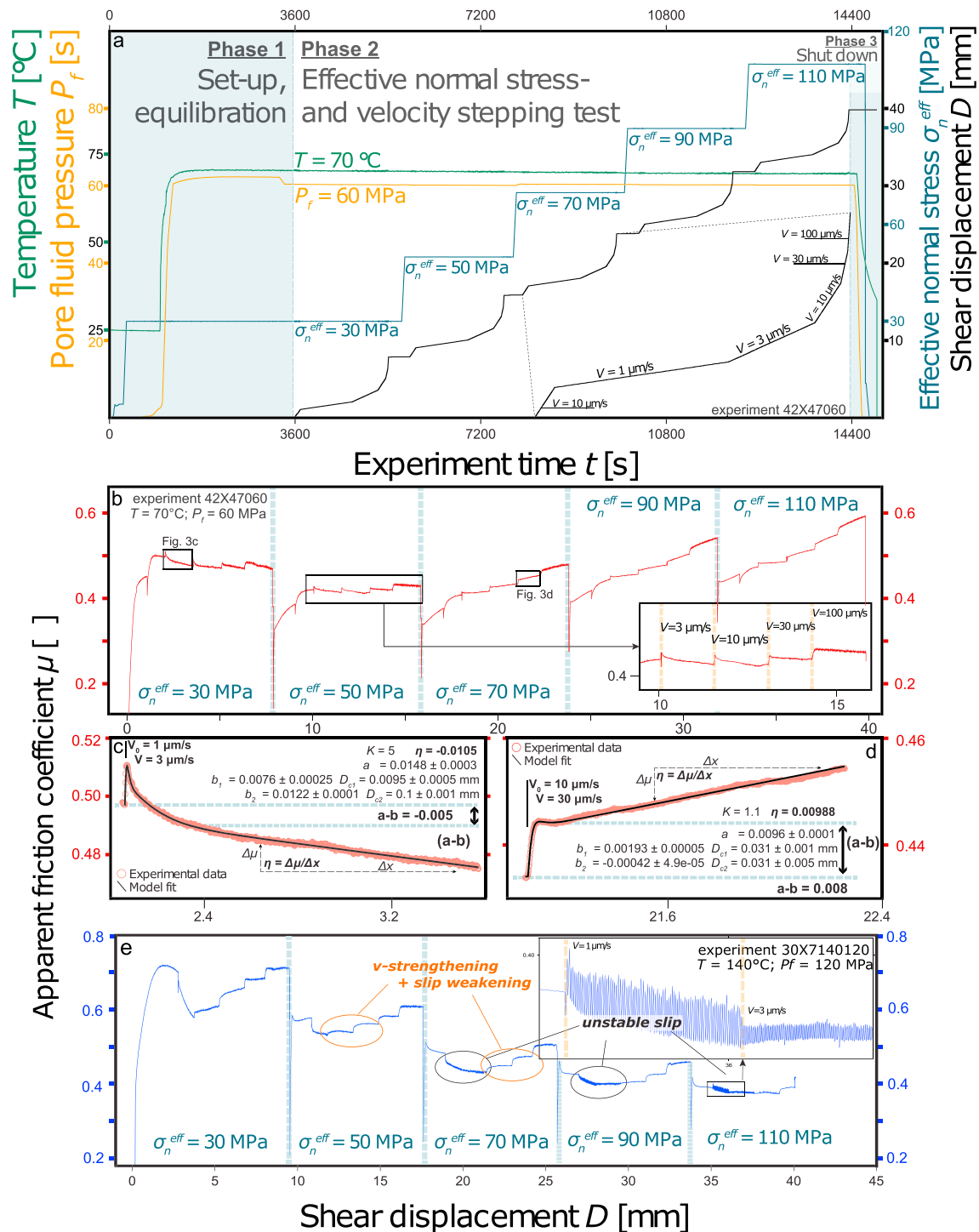
Figure 3. Examples of the complete course of two friction experiments (a–d) on clastic sample 42X-4 conducted at $T = 70\,°C$ and $P_f = 60$ MPa and (e) on pelagic calcareous sample 30X-7 conducted at $T = 140\,°C$ and $P_f = 120$ MPa. (a) Tracking of experimental parameters and consecutive shear displacements over time. (b) Evolution of the apparent friction coefficient. (c) Velocity-weakening- and (d) velocity-strengthening detail records of single velocity steps as outlined by black rectangles in (b); inversion results and definition of slip-weakening/hardening rate η. (e) Evolution of the apparent friction coefficient with highlighted instances of unstable slip (see also close-up in inset figure) and velocity-strengthening behavior accompanied by slip weakening.

pressure (P_f) were kept constant during each experiment and were varied systematically to establish a set of 2–7 differing experiments for each sample (Tables S1 and S2 in the supporting information). The temperature range explored encompasses experiments at room temperature, $T = 70\,°C$ and $T = 140\,°C$ to (1) cover the regime of the thermally controlled smectite-illite transition in clayey sediments and (2) purposely avoiding higher temperatures that are sufficient to trigger extensive metamorphism in nature. Pore fluid pressure was varied between $P_f = 20, 60$, and 120 MPa covering a wide range of hydrostatic and excess pore pressure conditions (Tables S1 and S2 in the supporting information).

Mechanical data were obtained in phase 2 during sequential shear displacements at consecutive effective normal stress states, starting with an initial load of $\sigma_n^{eff} = 30$ MPa and increasing load by steps of 20 MPa, or in cases 40 up to 110 MPa (Figure 3). At each effective normal stress step a sequence of increasing velocity (V) steps was carried out following the scheme 10-1-3-10-30-100 µm/s. Such low displacement rates are considered relevant for processes governing earthquake nucleation (Dieterich, 1979; Scholz, 1998). In order to perform effective normal stress steps, rotation of the motor was halted due to technical reasons, and the first velocity step after each increase at $V = 10$ µms served to establish a starting steady state microstructure.

To shut down the experiment, applied loads and conditions were removed in the reversed order during phase 3. After removal from the pressure vessel, the internal piston set was kept in an drying cabinet at 50 °C overnight to allow for an improved sample recovery.

3.3. Data Evaluation

Shear strength (τ) of the various sediments tested was normalized using the effective normal stress (σ_n^{eff}) and expressed in terms of the dimensionless apparent friction coefficient ($\mu = \tau/\sigma_n^{eff}$) assuming zero cohesion. This is consistent with the usage of simulated fault gouges to investigate fault reactivation processes, rather than incipient fault formation within undisturbed sediments. The concept of shear strength contrasts is often used to predict, which material is more prone to host deformation localization within a heterogenous and well-stratified sedimentary succession (see, e.g., Kopf, 2013; Kurzawski et al., 2016). Complementarily, the velocity dependence of sliding friction was explored and evaluated based on rate- and state-dependent friction (RSF) theory (Dieterich, 1979; Ruina, 1983):

$$\tau = [\; \mu_0 + \boldsymbol{a}\; ln(V/V_0) + \boldsymbol{b}\; ln(V_0\Theta/D_c)\;]\; \sigma_n^{eff} \tag{1}$$

where μ_0 constitutes a reference sliding friction value associated with a reference sliding velocity V_0 prior to an instantaneous step toward a new velocity V. D_c is the critical slip distance and the state variable Θ evolves according to the following:

$$d\Theta/dt = 1 - \Theta V/D_c. \tag{2}$$

Most importantly, the friction term includes the parameters a and b, which can be directly linked to material properties and microstructure if the underlying deformation mechanisms are known (Chen & Spiers, 2016). Together, they constitute the key parameter ($a - b$):

$$(a - b) = \Delta\mu/\Delta lnV \tag{3}$$

quantifying the frictional response to instantaneous displacement rate changes. Positive values in ($a - b$) imply a stronger resistance to shear movement toward higher displacement rates. Such behavior is termed velocity strengthening and facilitates stable aseismic sliding. As opposed to this, negative ($a - b$) values denote velocity weakening corresponding to potentially unstable frictional behavior. For comprehensive reviews on the topic the reader is referred to the work of Marone (1998a) and/or Scholz (1998). In general, experimental records display superimposed slip-hardening/weakening trends. These potentially constitute another material characteristic specified as slip-hardening/weakening rate $\eta = d\mu/dx$ (mm^{-1}) and were introduced as a potential mechanism for triggering slow earthquakes if initial velocity-strengthening behavior can be overcome by long-term slip weakening ($\eta < 0$) beyond a critical sliding distance W (Ikari, Marone, et al., 2013):

$$W = (b - a)\ln(V/V_0)\,\eta^{-1}. \tag{4}$$

We employed a least squares minimizing inverse modeling technique to fit an extended version of Dieterich's slowness law that applies two state variables to our experimental data (Reinen & Weeks, 1993; Figures 3c and 3d):

$$\mu = \mu_0 + a \ln(V/V_0) + b_1 \ln(V_0\Theta_1/D_{c1}) + b_2 \ln(V_0\Theta/D_{c2}). \tag{5}$$

The relation usually results in a better overall fit compared to the standard equation and is coupled with the elastic loading equation via the friction coefficient (μ), which constitutes the proportionality constant between shear stress (τ) and effective normal stress (σ_n^{eff}):

$$\tau = \mu * \sigma_n^{\text{eff}} + c, \tag{6}$$

where c is the cohesion. Another benefit of this numeric approach is the acquisition of model values for all other parameters involved, including critical slip distance (D_{ci}). Slip-weakening/hardening rate (η) and elastic stiffness (K), governing the transition from stable to unstable slip, are input parameters for the inversion and are therefore also acquired in this process. For the transition from stable to unstable slip, the stiffness of the loading system has to be lower than its critical value specified as

$$K < K_{\text{crit}} = \sigma_n^{\text{eff}}(b - a)/D_c. \tag{7}$$

All inversion results associated with this study are listed in the supporting information. In cases where the numerical inversion approach failed due to experimental artifacts or noisy records, values were hand picked using equation (3) and correction for slip-dependent weakening/hardening trends was applied manually.

3.4. Quantitative Whole Rock Mineralogy

Comprehensive mineralogical characterizations of our starting materials were carried out in terms of standard X-ray diffraction (XRD) analysis and complementary carbonate quantification by Bernard calcimetry, granulometry measurement, and wet-chemical amorphous silica content determination. Particle size was determined by a laser particle counter (LS230 BECKMANN COULTER), after samples being disintegrated in a sodium hexametaphosphate 1-g/L solution and dispersed. XRD analyses were performed on bulk powders prepared from dried and hand crushed original IODP samples using a Bruker D-4 Endeavor diffractometer mounted with a Vantec-1 detector using nickel-filtered Cu-Kα radiation. Scans were run from 2° to 65.146° 2θ, with a step size of 0.040° and 39.2 s per step. Standard locked coupled scan conditions were 40 kV and 30 mA. The identification of all minerals was performed using Bruker-AXS's DiffracPlus EVA software and the International Centre for Diffraction Data Powder Diffraction File 2008 database. The Fityk software©v0.9.8 (Wojdyr, 2010) was used for the decomposition of overlapped peaks to better identify the different phyllosilicate components. Furthermore, we employed an alkaline leaching method to determine opal contents in our samples (DeMaster, 1981). This wet-chemical dissolution technique is based on varyingly fast digestion rates of biogenic silica compared to aluminosilicates. When placed in an alkaline solution, the opal component of marine sediment is released most rapidly. The increase of the concentration of silica in the solution, however, is overprinted by a contribution from coexisting aluminosilicates, which manifests itself as a weak linear increase over time once all opal is consumed and hence can be subtracted (Müller & Schneider, 1993). For each sample, we dispersed approximately 40 mg of sediment in 400 g of 0.0316 M NaOH (pH 12.5) at 85 °C. The conditions are chosen to minimize the digestion of clay minerals (Schlüter & Rickert, 1998) and are adapted from Spinelli and Underwood (2004). Aliquots (6 ml) of the leachate were collected about 5, 15, 30, 60, 90, 120, 180, 270, and 360 min after digestion began. The concentration of silica in the leachate was determined by spectrophotometry. The contribution of opal to the leachate was determined by projecting the flattened tail of the concentration curve back to time $t = 0$. In determining the weight percent of opal in the bulk samples, we assumed the water content of opal to be 11% by weight (Kastner et al., 1981).

4. Sample Descriptions

4.1. Large-Scale Lithostratigraphy

Representative samples chosen for ring shear tests cover a wide range of lithological units from the frontal prism, the upper and middle slopes of the upper Caribbean Plate and the downgoing Cocos Plate. In Figure 1 the chosen samples are indicated by arrows next to the lithostratigraphic columns. For detailed descriptions the reader is referred to the Proceedings of the IODP Expeditions 334 and 344 (Harris et al., 2013a, 2013b; Expedition 334 Scientists, 2012a, 2012b).

4.1.1. Incoming Plate Site U1414 — Unit IB (Sample 14H-6)

Unit I consists of unconsolidated massive dark greenish-gray (silty) clay with abundant foraminifera and is divided into two subunits. Whereas Subunit IA (0–78.3 m below seafloor [bsf]) contains significant amounts

of sand layers and terrigenous material such as quartz, feldspar, and lithic fragments, these components are much sparser in Subunit IB (78.3–145.34 m bsf), which exhibits a clear hemipelagic character and contains abundant calcareous nannofossils. Biogenic material, in general, and components such as radiolarians, foraminifers, and sponge spicules become more dominant in the clayey matrix, and the unit is denoted as light greenish-gray calcareous nannofossil-rich silty clay. Sample 14H-6 originates from the incoming plate Site U1414 (Figure 1) and was recovered from a depth of 124 m bsf (Subunit IB).

4.1.2. Incoming Plate Site U1414—Unit II (Samples 20H-2, 25X-4 and 30X-7)

Unit II (145.34–309.37 m bsf, Figure 1) comprises pelagic sediments and distinguishes itself from Unit I by its abundant biogenic content. This characteristic is clearly reflected in the change in color to light green, gray, or even white. The sediment contains >70% biogenic components, such as spicules, diatoms, radiolarians, and nannofossils. As a general rule, calcareous components decrease and silicious components increase with respect to bore hole depth. Accessory minerals, such as feldspar, pyroxene, calcite, and opaque minerals, occur throughout the entire section. Subunit IIA (145.34–200.01 m bsf), where sample 20H-2 (174.32 m bsf) originates from, consists of massive, light green calcareous ooze. It further contains smectite and zeolite, which do not occur toward deeper parts of the sequence. Subunit IIB (200.01–309.37 m bsf) comprises an alternating sequence of dark grayish to greenish silty clayey calcareous ooze (sample 25X-4, 224.97 m bsf) and white calcareous ooze containing abundant sponge spicules (sample 30X-7, 275.59 m bsf). The amount of diagenetic opal increases with depth.

4.1.3. Frontal Prism Site U1412—Unit I (Sample 2H-1)

Unit I (0.00–204.74 m bsf) of the frontal prism Site U1412 is dominated by terrigenous clay sediments. The material is described as massive dark greenish-gray clay intercalated with silty clay horizons. Besides clay minerals, the main silty accessory matrix components comprise feldspar and lithic fragments. Nannofossils, diatoms, and fragments of diatoms and radiolarians are common biogenic constituents. Sample 2H-1 was recovered from a depth of 7.25 m bsf.

4.1.4. Frontal Prism Site U1412—Unit III (Sample 8R-6)

At the frontal prism Site U1412 Unit III represents a well-sorted clayey siltstone (Sample 8R-6, 365.09 m bsf) with minor interlayered sandstone. Sandstone horizons occur more abundantly toward deeper portions of the hole. Also, organic material that is generally sparse increases with depth. Dominant matrix constituents are clay minerals, abundant feldspar and rock fragments, biogenic components, and various accessory minerals.

4.1.5. Midslope Site U1378—Unit IIA (Samples 24X-4 and 42X-4)

Unit II at the midslope Site U1378 consists of a monotonous sequence of terrigenous sediments dominated by olive-green clayey silt(stone) and silty clay(stone; Subunit IIA, Samples 24X-4, 194.8 m bsf and 42X-4, 348.75 m bsf) with minor occurrences of sand(stone) layers (Subunit IIB). In contrast to the incoming plate and frontal prism sites, sediments are rather firm and more consolidated. Main constituents are clay minerals, and feldspar and lithic fragments in the silt fraction. Clay minerals which have been observed in all clay-rich samples are kaolinite, chlorite/smectite (C/S), and illite/smectite (I/S). Biogenic components are rare.

4.1.6. Upper Slope Site U1379—Unit III (Sample 101X-5)

At the upper slope Site U1379 Unit III (651–880.07 m bsf) consists mainly of olive-green silty sands and sandstones. Coarse sandy deposits are reported to make up to 64% of the total unit thickness, alternating with finer hemipelagic deposits (Sample 101X-5, 866.95 m bsf). Main components are feldspar and lithic fragments. The most abundant accessory component is chlorite, followed by volcanic glass, opaque minerals, and amphibole.

4.2. Semiquantitative Whole Rock Mineralogy

Quantitative sample compositions as derived from XRD analysis and complementary wet-chemical leaching are in line with the previous descriptions and are summarized in Table 1. Quartz values represent combined amounts of crystallized biogenic material and clastic rock fragments. Identified minerals with unspecified amounts are indicated by x. Based on those results, two groups of samples can be defined. The first group comprises samples that contain no significant amounts of clay minerals but rather show large amounts of calcite (1414-30X7, 1414-20H2, and 1414-25X4). The second group corresponds to samples showing total clay contents (chlorite, illite/smectite, and smectite/chlorite) of about 20–30 wt % (1412-2H1, 1378-42X4, 1414-14H6, and 1379-101X5). Opal is present in all samples in moderate amounts of ≈5 wt %.

5. Experimental Results

5.1. Frictional Strength

Peak or yield frictional strength ($\mu_{p/y}$), respectively, were determined from the run-in velocity step at $v = 10$ μm/s for each effective normal stress step. Variations in frictional strength as a function of temperature

Table 1
Sample Compositions From XRD Analysis, Bernard Calcimetry and Wet-Chemical Leaching

SAMPLE	Calcite (wt %)	Qtz + Fsp (wt %)	Clay total (wt %)	Zeolite (wt %)	Opal (wt %)
1414-30X7	>90	<5	traces	traces	4
1414-20H2	45	50–55	traces	traces	2
1414-25X4	25	70–75	traces	traces	3
1414-14H6	20	40–45	30–35	<5	3
1412-2H1	15	40–45	30–35	<5	5
1412-8R6	15	35–40	35–40	traces	6
1378-24X4	10	x	x	x	3
1378-42X4	5	50–55	35–40	<5	5
1379-101X5	<5	50	35–40	<5	4

Note. Qtz = quartz; Fsp = feldspar; XRD = X-ray diffraction.

(T), pore fluid pressure (P_f), and effective normal stress (σ_n^{eff}) are more or less pronounced depending on sample composition and especially the carbonate content (Figure 4). Carbonate contents were derived from the IODP LIMS Reports online repository (http://web.iodp.tamu.edu/UWQ). Measurements were conducted by the shipboard parties of the IODP Expeditions 334 and 344 on board *DV JOIDES Resolution*, which applied ion chromatography. Additionally, XRD analysis and calcimetry results on our samples are presented in Table 1.
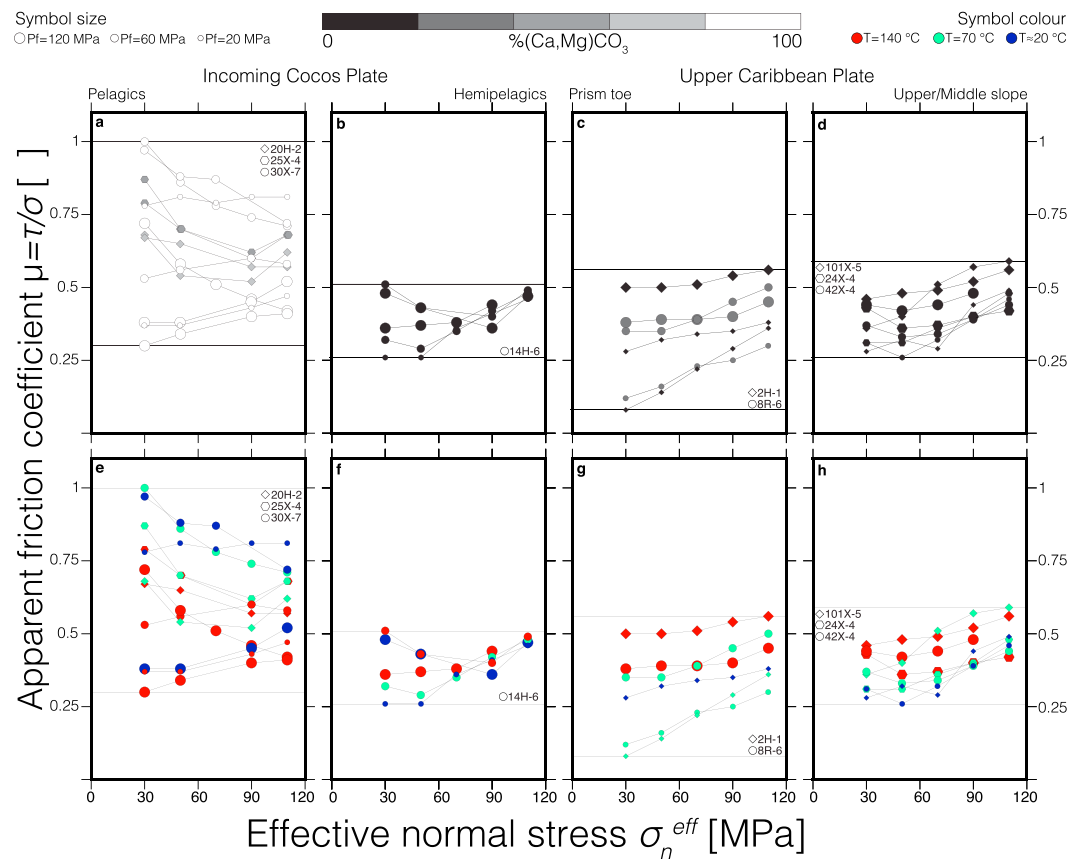

Figure 4. Evolution of frictional strength with effective normal stress depending on changes in carbonate content as outlined by gray scale (a–d) and temperature (e–h). Symbol colors represent different temperatures due to the scheme in the upper right corner. Symbol size represents different pore pressure states as indicated in the upper left corner. For better comparison the corresponding ranges are marked by horizontal lines in each subfigure, combining results for samples originating from either the same tectonic positions (e.g., frontal prism vs. upper/middle slope) and/or depositional realms (e.g., pelagics vs. hemipelagics). Note the extraordinarily wide range of highly calcareous samples.

5.1.1. Incoming Plate Pelagics

Peak/yield friction of carbonate-rich pelagics from the incoming plate are highly sensitive to applied experimental conditions, varying between $0.3 \leq \mu_{p/y} \leq 1$. The pelagics are predominantly strong with $\mu_{p/y} \geq 0.6$ and, as a general trend, tend to be weak at high temperatures and pore fluid pressures (Figures 4a and 4e). In fact, all experiments resulting in low apparent friction coefficients below $\mu_{p/y} \leq 0.5$ were conducted at $T = 140\,°C$, except for one experiment at room temperature and high pore fluid pressure of $P_f = 120$ MPa. Peak/yield values resulting from all other room temperature experiments cluster at the higher end of the frictional strength spectrum, together with those from experiments conducted at $T = 70\,°C$ (Figures 4a and 4e). All of those experiments represent low to intermediate pore pressure states. Two experiments on calcareous ooze gouge (sample 30X-7) conducted at identical conditions ($T = 140\,°C$, $P_f = 120$ MPa) show an extreme deviation in terms of peak/yield frictional strength at $\sigma_n^{\mathrm{eff}} = 30$ MPa, which gradually tapers off with increasing effective normal stress. These data reveal the existence of at least one further parameter, which significantly affects the apparent friction coefficient of carbonates that was not controlled in our experiments. We comment on this later in section 6. Finally, the data suggest that overall frictional sliding strength is somehow related to the carbonate content of the samples. All calcareous pelagics consistently show higher apparent friction coefficients than samples with low carbonate content. However, there is no systematic correlation with changing carbonate content. Sample 20H-2, showing the second highest carbonate content of > 60 wt%, reaches only intermediate frictional strength values between $0.52 \leq \mu_{p/y} \leq 0.68$. Sample 25X-4, consisting of ≈ 45 wt % carbonates, however, shows the second highest frictional strength in the range of $0.6 \leq \mu_{p/y} \leq 0.87$ (Figure 4a).

5.1.2. Incoming Plate Hemipelagics

Hemipelagic silty clay (sample 14H-6) from the overlying portion of the incoming sediment section is weak in terms of sliding friction and more importantly shows only minor variations in frictional strength in response to changes in experimental conditions. Apparent peak/yield friction coefficients cover the narrow range between $0.26 \leq \mu_{p/y} \leq 0.51$ (Figures 4b and 4f). Despite these little variations, the samples exhibit some minor positive trends with increasing temperature, pore pressure, and effective normal stress. Effects of temperature and pore fluid pressure are more pronounced at low effective normal stress states up to 50 MPa, whereas above 50 MPa, effective normal stress itself is the crucial parameter resulting in a positive trend in frictional strength. In the following, systematics at low effective normal stress are exemplarily described for the lowest effective normal stress step at $\sigma_n^{\mathrm{eff}} = 30$ MPa. The samples exhibit their lowest frictional strength at room temperature and low pore fluid of $P_f = 20$ MPa. Increasing temperature and pore fluid pressure simultaneously causes a slight increase in the apparent friction coefficient from $\mu_{p/y} = 0.26$ over 0.32 at $T = 70\,°C$ and $P_f = 60$ MPa to 0.36 at $T = 140\,°C$ and $P_f = 120$ MPa , suggesting a positive relation for the combined effect of the two parameters. Separate variations in only one of the parameters, however, reveal a more complex interdependency. At room temperature, an increase in pore fluid pressure from $P_f = 20$ to 120 MPa resulted in significant frictional strengthening from $\mu_{p/y} = 0.26$ to 0.48. By contrast, increasing pore fluid pressure by 60 MPa at $T = 140\,°C$ leads to reduction of frictional strength from $\mu_{p/y} = 0.51$ to 0.36.

5.1.3. Frontal Prism Clastics

Similar to pelagics, fine-grained clastic slope sediments from the frontal prism Site U1412 in the vicinity of the MAT (clayey silt sample 2H-1 and silty clay sample 8R-6, respectively) cover a relatively broad range of peak/yield apparent friction coefficients. These samples, however, encompass the lower end of the frictional strength spectrum ranging between $0.08 \leq \mu_{p/y} \leq 0.56$ including the lowest apparent peak/yield friction coefficients of the entire data set at $T = 70\,°C$, $P_f = 20$ MPa and $\sigma_n^{eff} = 30$ MPa (Figures 4c and 4g). Compared to calcareous pelagic sediments, these samples show a reverse dependency of sliding friction on temperature and pore fluid pressure. The highest values in apparent friction coefficient coincide with high temperature and pore fluid pressure conditions. Two experiments on silty clay (sample 8R-6), both conducted at $T = 70\,°C$, reveal an increase in peak/yield frictional strength with respect to increasing pore fluid pressure. Between these two experiments only pore fluid pressure was increased by 40 MPa from $P_f = 20$ to 60 MPa, resulting in a consistent increase in sliding friction by $\Delta\mu_{p/y} \approx 0.2$ for each effective normal stress step.

5.1.4. Upper and Middle Slope Clastics

Clastic sediments from the upper and middle slope sites, respectively, consistently exhibit very low carbonate contents $<< 10\%$ and show relatively unvaried frictional strength records, covering the intermediate range of $0.26 \leq \mu_{p/y} \leq 0.59$ (Figures 4d and 4h). The slope sediments show positive trends with increasing effective normal stress. The samples also exhibit a positive strength relation to the combined effects of increasing temperature and pore fluid pressure, especially at low effective normal stress.
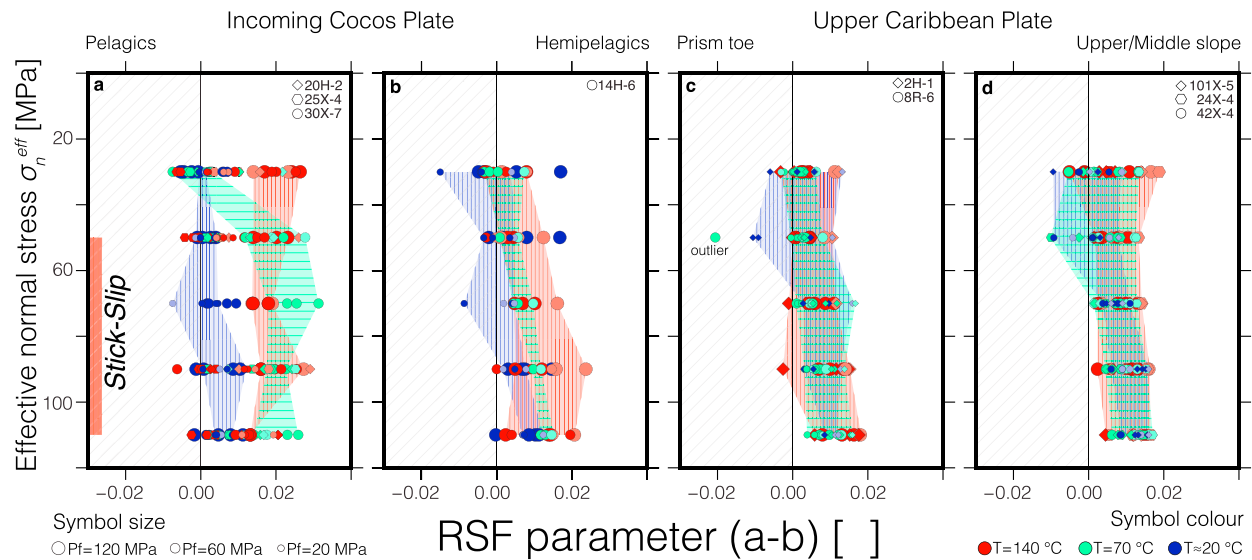
Figure 5. Rate and state parameter ($a - b$). The domain representing potentially unstable velocity-weakening behavior (($a - b$) < 0) is outlined by gray hatching in all subfigures. Data points in pale colors and dashed symbols represent hand picked values using equation (3). (a–d) Data sets representing combined temperature and pore fluid pressure increases ((RT/20 MPa) ⇒ (70 °C/60 MPa) ⇒ (140 °C/120 MPa)) are highlighted in respective background colors and hatching. In Figure 5a, only the records related to experiments on calcareous ooze sample 30X-7 are emphasized. Records for all slope sediments are presented together due to their similarity (Figures 5c and 5d). The range of stick slip occurrence, implying negative values in ($a - b$) is marked by a side bar. RFS = rate- and state-dependent friction.

5.2. Frictional Stability

Frictional stability of all samples tested is shown in terms of the RSF parameter ($a - b$) as a function of effective normal stress (Figure 5).

5.2.1. Incoming Plate Sediments

Gouges prepared from calcareous pelagic sediments (samples 20H-2, 25X-4, and 30X-7; Figure 5a) and hemipelagic silty clay (sample 14H-6; Figure 5b) from the incoming sediment section show important differences with respect to frictional stability. Silty clay gouge shows decreasing ($a - b$) values toward lower effective normal stress states within the range of $0.002 \leq (a-b) \leq 0.02$ at $\sigma_n^{\text{eff}} = 110$ MPa to $-0.015 \leq (a-b) \leq 0.008$ at $\sigma_n^{\text{eff}} = 30$ MPa, except for one experiment that was conducted to explore elevated pore fluid pressure (60 MPa) at room temperature (Figure 5b). This experiment shows a stabilizing effect of pore pressure at low effective normal stress, shifting ($a - b$) toward higher values (($a - b$) ≤ 0.017 at $\sigma_n^{\text{eff}} = 30$ MPa). In all other experiments, velocity-weakening behavior is strongest at the lowest effective normal stress step ($\sigma_n^{\text{eff}} = 30$ MPa), where it occurs at all temperatures and up to $\sigma_n^{\text{eff}} = 70$ MPa at room temperature. The samples tend to velocity strengthen at a combined temperature and pore fluid pressure increase (Figure 5b, color shading).

Frictional stability of gouges prepared from calcareous pelagic sediments from greater depth strongly depends on the carbonate content. Sample 25X-4 with the lowest carbonate content (≈45%; Figure 4a) encompasses negative ($a-b$) values in both experiments, markedly at low effective normal stress where velocity weakening occurs at $T = 70$ and 140 °C (Figure 5a). The sample shows a consistent shift toward lower ($a-b$) values in the 140 °C experiment. By contrast, sample 20H-2, consisting of ≈60% carbonate, shows no obvious dependency on any parameter and displays almost exclusively velocity-strengthening behavior. Calcareous ooze sample 30X-7 contains ≈90% carbonate and exhibits the most distinctive frictional behavior (Figure 5a). The sample is mostly velocity neutral at room temperature and $P_f = 20$ MPa and shows a slight tendency to velocity strengthen at the highest effective normal stresses tested. At 70 °C and $P_f = 60$ MPa, negative ($a - b$) values were only recorded at the lowest effective normal stress step ($-0.003 \leq (a - b) \leq 0.003$; 30 MPa), whereas strong velocity-strengthening behavior ($0.012 \leq (a - b) \leq 0.031$) occurs in all other stress steps. At the highest conditions tested (140 °C and $P_f = 120$ MPa), calcareous ooze gouge is velocity strengthening ($0.013 \leq (a - b) \leq 0.026$) at high-velocity steps but show frictionally unstable behavior indicated by stick-slip events at low velocity steps (Figure 5a). Unstable behavior covers a broader velocity range with increasing effective normal stress. It was not possible to obtain constitutive RSF parameters for instances of unstable slip via inversion. Therefore, the range of stick slip occurrence in terms of effective normal stress is marked by a
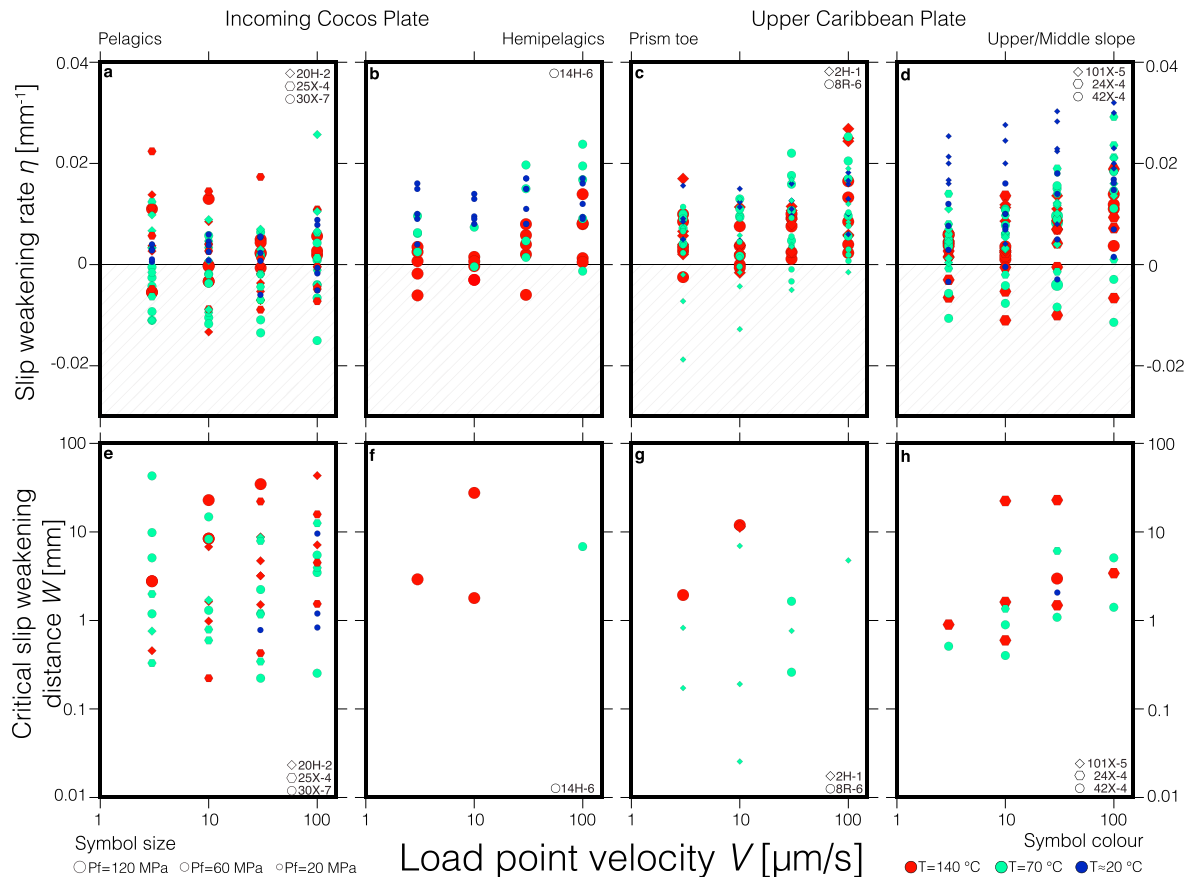
Figure 6. (a–d) Slip-weakening/hardening rate η and (e–h) critical slip-weakening distance W as a function of up-step load point velocity V. The range of slip-weakening behavior ($\eta < 0$) potentially triggering slow slip events is highlighted by a shaded background in subfigures (a)–(d). Symbol size and color are defined below panels (e) and (h), respectively. Note that slip weakening appears to be temperature controlled, especially in clayey hemipelagics (panels b) and most likely occurs in calcareous pelagics (panels a and e). Material from the prism toe region shows the shortest critical slip-weakening distances (panel g).

side bar. More detailed results of experiments on this exact sample (and hemipelagic silty clay sample 14H-6) are described in Kurzawski et al. (2016).

5.2.2. Slope Sediments

Simulated gouges prepared from all overriding plate sites show very similar behavior in terms of frictional stability (Figures 5c and 5d). Apart from a few exceptions, all samples exhibit a slightly broader range of ($a - b$) data spanning both, positive and negative values at their two lowest effective normal stress steps. With increasing σ_n^{eff} this range becomes smaller and shifts to the velocity-strengthening side, apart from sample 2H-1 deformed at 140 °C. The trend of slightly increasing values toward higher effective normal stress is not affected by temperature and pore fluid pressure changes.

5.3. Slip-Weakening/Hardening Rates

Long-term slip dependence of sliding friction was measured from the linear part of each velocity step, representing steady state changes in friction coefficient with displacement ($\eta = d\mu/dx$ [mm^{-1}]). Positive values in η represent long-term slip hardening, while slip-weakening behavior is revealed by negative values (Figures 6a–6d) and can result in net weakening and slip instability (Ikari, Marone, et al., 2013). This linear hardening/weakening behavior might be affected by material loss during the course of the experiments, which might affect the measured friction by getting jammed in between the piston and the confining rings, and our presented results will be discussed under consideration of the evolution of experimental gouge layer thickness. In the following we will focus on key observations and will not describe the specific behavior of each sample in detail.

Experimental results show that slip-weakening behavior is thermally controlled. With only few exceptions, room temperature experiments consistently show slip-hardening records ($\eta > 0$, Figures 6a–6d), including

the highest values of the entire data set of up to $\eta \approx 0.03$ mm^{-1} from upper slope clastics (Figure 6d). By contrast, slip weakening ($\eta < 0$) is almost exclusively characteristic of heated experiments and is displayed in the records of all samples tested. Its occurrence and especially its dependency on applied experimental conditions vary with sample composition.

5.3.1. Incoming Plate Sediments

Pelagic and hemipelagic incoming sediments display distinct differences in slip rate behavior. Pelagic sediments show extensive slip-weakening records making up approximately 50% of their entire slip dependence spectrum (Figure 6a). Strongest slip weakening ($\eta \approx -0.015$ mm^{-1}) occurs at $T = 70°C$ and all sliding velocities for all pelagic samples (Figure 6a). There are, however, no obvious trends in terms of temperature, sliding velocity or effective normal stress, and the data appear somewhat scattered.

Silty clay (sample 14H-6) is predominantly slip hardening with invariantly high rates up to $\eta = 0.017$ mm^{-1} at all velocities and room temperature (Figure 6b). Highest values occur at high effective normal stress. The hardening rate ranges between neutral or slight slip hardening at $T = 70°C$. It exhibits strong slip hardening ($\eta \approx 0.02$ mm^{-1}) at highest velocities. Slight slip-weakening behavior (-0.006 mm$^{-1} < \eta < -0.002$ mm^{-1}) is recorded in experiments at $T = 140°C$, showing a trend to stronger slip weakening toward decreasing load point velocities.

5.3.2. Prism Toe Clastics and Slope Sediments

Prism toe clastics and slope sediments preferentially show slip-hardening behavior ($\eta \leq\approx 0.025$, Figures 6c and 6d; $\eta \leq\approx 0.03$, Figure 6d). Clay sample 2H-1 from the frontal prism Site U1412, however, also exhibits strong slip weakening at $T = 70°C$ and $P_f = 20$ MPa ($\eta \geq -0.019$ mm^{-1}; Figure 6c). Midslope and upper slope sediments display a wide range of slip dependence within the range $-0.011 \leq \eta \leq 0.03$ mm^{-1} (Figure 6d), consistent with previous observations, such as high slip-hardening rates at room temperature and some slip weakening in heated experiments.

5.4. Slip-Weakening Distances

The so-called critical slip-weakening distances (W) result from the link of velocity and slip dependence (equation (4)) and were suggested to illustrate the potential to initiate unstable slow slip via slip weakening within the subduction channel (Ikari, Marone, et al., 2013; Figures 6e–6h). Such behavior is favored, if materials (1) exhibit velocity neutral or only weak velocity-strengthening behavior (($a - b$) $\approx +0$) to constitute a small barrier that has to be overcome and/or (2) require only a small amount of displacement for friction to fall below its initial value ($\mu < \mu_0$; small W). Note how the amount of data in the lower panels is decimated in comparison to total slip-weakening occurrences ($\eta < 0$; shaded areas in Figures 6a–6d). W is always positive, as it characterizes frictional behavior that is both velocity strengthening and slip weakening. W values obtained here, especially those giving large numbers on the scale of several millimeters to several centimeters, have to be handled with care as they assume unchanged hardening/weakening rates over considerably larger amounts of displacement than actually measured in velocity steps.

5.4.1. Incoming Plate Sediments

Calcareous pelagics (Figure 6e) are the more likely candidates to trigger slip-weakening instability compared to hemipelagic silty clay (Figure 6f). The large amount of data points comprising very low W values ($W \geq\approx 0.2$ mm) and also the wide range of conditions allowing such behavior favor carbonates. Critical slip-weakening distances can be observed for all experimental conditions but predominently at $T = 70$ and $140°C$. By contrast, minimum critical slip-weakening distances in hemipelagic silty clay are almost 1 order of magnitude higher ($W \geq\approx 1.8$ mm) and mostly require temperatures higher than $T = 70°C$ (Figure 6f).

5.4.2. Slope Sediments

Samples from the frontal prism exhibit the lowest critical slip distances of the data set ($W \geq\approx 0.02$ mm; Figure 6g) and are prone to slip-weakening instabilities in experiments at $T = 70°C$ and $P_f = 20$ MPa. Sediments from the middle and upper slopes show intermediate W values.

6. Discussion

The experimental results of this study shed light on the dependence of fault slip modes along the Costa Rican plate boundary décollement, including shallow aseismic creep, slow slip, and seismic rupture, on the frictional behavior of the various subducted sediments. In the following we intend to elucidate the frictional behavior based on the rotary shear tests at hydrothermal conditions. We also discuss the significance of carbonate gouge for shallow seismicity and the implications of our experimental results for subduction plate boundary deformation in general.

6.1. Frictional Strength

Sliding frictional strength of the investigated sediments is highly variable and gets further complicated under changing ambient conditions during subduction over time. Variations in frictional strength and especially the evolution of strength contrast determine which of the different sediments in the subduction channel is prone to localize strain and host the décollement.

Apparent friction coefficients of calcareous sediments are extremely sensitive to ambient conditions such as effective normal stress, temperature, and pore fluid pressure, particularly when compared to clastic sediments, which show a more uniform frictional strength (Figure 4). This means that strength contrasts between different materials within the subduction channel vary as a function of burial depth with strong implications for the localization of the décollement and associated faults, which are expected to localize within the weakest material present. Our data support the findings of Kopf (2013) who investigated incoming plate sediments from Ocean Drilling Program Leg 170 in rotary shear at room temperature and showed that the frontal tip of the subduction thrust cuts into the weakest material ($\mu = 0.16 - 0.25$). Our sample set comprises hemipelagics from the incoming plate as well as slope sediments from the prism toe (samples 1414-14H6 and 1412-2H1, respectively), which show comparably low frictional strength at conditions for shallow subduction (Figure 4b/4f and Figure 4c/4g). The lowest sliding friction values ($\mu < 0.1$), however, are exhibited by prism toe clastics at 70 °C. Toward greater burial depths the clastic sediments tend to strengthen with increasing effective normal stress and are less affected by changes in temperature and pore fluid pressure, as opposed to calcareous lithologies, which show significant variations including even a weakening with increasing effective normal stress. The dramatic weakening as a function of temperature and pore fluid pressure might promote earthquake nucleation within carbonates at depth and was explored in detail by Kurzawski et al. (2016) for variations in internal friction. The apparent friction coefficient is strictly speaking only characteristic of faults in movement and not relevant for earthquake nucleation processes, as it neglects cohesion and stationary restrengthening. Hence, any fault restrengthening due to frictional healing or veining during the seismic cycle that was shown to significantly affect fault friction in numerous studies (Beeler et al., 1994; Carpenter et al., 2016; Chen et al., 2015; Dieterich, 1972; Marone, 1998b; Marone & Saffer, 2015) is not accurately described. Also, it was recently shown that healing during holds prior to reshearing of carbonate gouge might result in a shift in the RSF parameter ($a - b$) and additionally affect the frictional stability (Carpenter et al., 2016; Chen et al., 2015).

Extremely low friction coefficients ($\mu < 0.1$) recorded in prism toe clastics at 70 °C (Figure 4c/4g) may be caused by trapped and pressurized fluid lubricating the faces of sheet silicates. The permeability of clay-rich sediments is very low compared to any other sediment, meaning that such lithologies are much more susceptible for the occurrence of pore pressure transients. Again, systematic studies are required to quantify these effects as they might be relevant for postseismic relaxation and/or triggered movements associated with Coulomb stress transfer.

6.2. Pore Fluid Pressure and Locking Degree

The locking degree of the plate boundary fault is one important model parameter characterizing the seismogenic potential for megathrust earthquakes. A fully locked plate boundary interface is believed to facilitate the buildup of elastic strain, which can be released in a large seismic event. According to the stiffness equation (equation (7)), an increasing pore fluid pressure is expected to cause a drop in critical stiffness, thereby counteracting any frictional instability. Hence, an elevated pore fluid pressure has a stabilizing and, therefore, unlocking effect on the plate boundary interface. In a subset of our experiments we investigated the individual effect of pore fluid pressure variations on the frictional stability of distinct lithologies as displayed by the RSF parameter ($a - b$). For this purpose, pelagic calcareous ooze gouge, hemipelagic silty clay gouge, and prism toe clastics gouge were deformed at two to three different pore fluid pressure and temperature states (Figure 7). Some of these tests encompass extreme experimental boundary conditions (like the test at $T = 140$ °C and $P_f = 20$ MPa) presumably not representative for the natural situation but important to illuminate the full parameter space. The resulting shift toward higher ($a - b$) values, that is, a more pronounced velocity-strengthening behavior, indicates a frictional stabilization with increasing pore fluid pressure. This effect is strongest within hemipelagic silty clay gouge at room temperature and especially at low effective normal stress (Figure 7b). It also occurs at high temperature (Figure 7e) and is characteristic of the prism toe clastic gouge, as well, though less pronounced (Figure 7c). Calcareous ooze gouge, however, significantly deviates from this trend. At $T = 140$ °C, the opposite dependency is preferentially encountered (Figure 7d), namely, a shift toward velocity-weakening behavior and stick-slip occurrence implying negative ($a - b$) values. Frictional
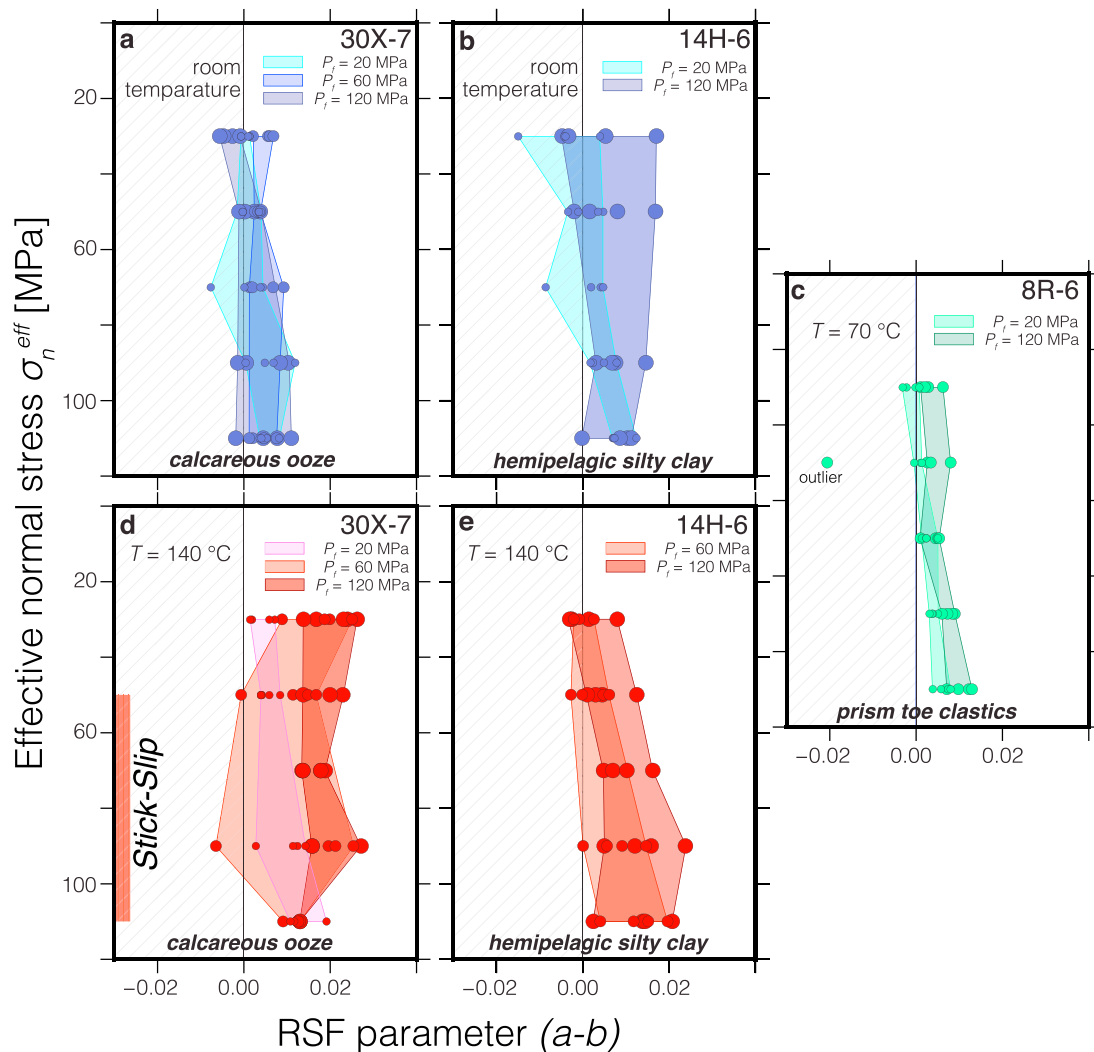
Figure 7. (a – e) Dependence of frictional stabilization/destabilization on pore fluid pressure variations. Color coded polygons mark ranges of corresponding data points recorded at identical pore fluid pressure states following the legends depicted in each respective subfigure. Pore fluid pressure related frictional stabilization as indicated by a shift toward larger $(a − b)$ values occurs in the majority of cases and especially in clayey gouges. Note the frictional destabilizing effect in calcareous ooze gouge at 140 °C. RSF = rate- and state-dependent friction.

destabilization becomes stronger toward higher effective normal stress states as expected from the critical stiffness equation, where slip instability also covers an increasingly broad velocity range. A shift to negative $(a − b)$ values also occurs at room temperature and low effective normal stress. These results clearly demonstrate that the general assumption of a pore pressure related stabilization of the plate boundary fault zone constitutes a vast oversimplification because it does not take into account the possible effects of pore fluid pressure on the shearing process itself. Rather, in the critical stiffness equation, pore fluid pressure only plays a mechanical role by lowering the effective normal stress. Our experimental results show that besides this mechanical effect, the pore fluid pressure has a direct effect on the velocity dependence of friction, that is, $(a − b)$. The presence of overpressurized fluid might result in a quite different outcome depending on the specific combination of present rock type and ambient conditions. Further detailed parameter studies are needed to better understand the conditions for frictional (de-)stabilization and locking of plate boundary faults.

6.3. Shallow Slow Slip Generation

The occurrence of plate boundary slip transients such as SSEs, low-frequency earthquakes, very low frequency earthquakes, and tremor was believed to be restricted to the depth range between 30 and 50 km, that is, toward the downdip end of the upper seismogenic zone. A wealth of seismological and geodetic observations along well-instrumented convergent margins summarized by Saffer and Wallace (2015) suggests

that near-trench shallow slow earthquakes are also a common phenomenon occurring in most subduction zones on the planet. However, the spatial range and ambient conditions of shallow slow slip vary significantly between individual subduction zones asking for common and varying causes. Elevated temperature, compaction-related pore space reduction, and fluid release due to early diagenetic mineral dehydration reactions were ruled out as primary factors controlling shallow slip (Saffer & Wallace, 2015, and references therin). It has been suggested though that source regions of shallow slow slip coincide with zones of the most several pore fluid overpressure along the plate interface (Saffer & Wallace, 2015).

Recently, an alternative mechanism for the possible generation of SSEs was proposed by Ikari, Marone, et al. (2013). This mechanism invokes linear slip weakening in combination with (mildly) velocity-strengthening behavior and was inspired by the observation of different slip-hardening/weakening trends observed in experiments on clay-rich samples from IODP drilling in the Nankai through. Traditionally, these trends are removed from the inversion of the data to obtain the response due to a perturbation of load point velocity by substracting linear fits, with the argument that these are backgrounds trends and that as such they are unrelated to the transient effects of the velocity perturbation (Blanpied et al., 1998). The weakening/hardening is believed to be result of an evolution of the microstructure, for example, the evolution of localized shear bands such as R1 or boundary shears (Blanpied et al., 1998; Ikari, Marone, et al., 2013). Ikari, Marone, et al. (2013) argue that the removed trends are in fact part of the material behavior and should as such be taken into account when we apply our friction data to nature. In order to do so, these authors defined a critical sliding distance W (not to be confused with the seismological or high-velocity friction slip-weakening distance) as specified in equation (4). It was argued that if W is small, linear slip weakening should dominate fault behavior and accelerated slip is possible. However, there are a number of issues to consider here. First, any weakening or hardening trend observed in experiments could be a result of experimental artifacts. In direct shear configurations in a triaxial setup, this could be a change in load-bearing area with displacement. In our rotary shear configuration, synshear material loss might produce two types of artifacts: (1) experimental gouges displaying heterogeneous grain size distributions with a significant clay fraction, such as our silty clay gouges, are expected to progressively release clays into suspension within the pore water and might be squeezed out from in between the internal pistons. This effect should enhance gouge layer thinning compared to other lithologies, and cause slip hardening due to bulk compositions enriched in quartz and feldspar (type I artifact). (2) The loss of material implies thinning of the experimental gouge layer, leading to a thinning rate-dependent strain rate increase. Consequently, velocity-weakening material might show apparent slip-weakening behavior, and as opposed to this, velocity-strengthening material might apparently slip harden (type II artifact). This second effect is expected to be visible in monomict materials such as the calcareous ooze gouge used in our experiments. Figure 8 summarizes the evolution of experimental gouge layer thickness under load in representative experiments on pelagic calcareous ooze gouge and hemipelagic silty clay gouge. Slip-hardening/weakening rates are correlated with the corresponding gouge layer thickness.

Under load, there is a significant difference in starting layer thickness between calcareous ooze gouge ($\approx 950\mu m < h < 1,100\mu m$) and silty clay gouge ($\approx 650\mu m < h < 700\mu m$). This is easily explained by the higher compressibility of clays and implies considerably higher strain rates in experiments on silty clay gouges. Thinning trends, however, are surprisingly similar in both materials, except for much stronger thinning in the calcareous ooze gouge at room temperature. Taking into account, that our calcareous ooze gouge dominantly consists of clay-sized calcite particles (Kurzawski et al., 2016; i.e., particles that preferentially suspend in the pore fluid), comparable thinning trends are indeed logical. It follows that strain hardening/weakening rates were acquired at different underlying strain rates, but the shift in strain rate remains more or less constant in the course of the experiments. Thinning rates are high during the run-in velocity step after each effective normal stress step but decrease during ongoing shear (Figure 8). Therefore, the contribution of the type II artifact to acquired strain hardening/weakening rates seems to be negligible in most cases. In general, η shows positive trends as a function of displacement, that is, decreasing gouge layer thickness, and effective normal stress (Figure 8). Much of the slip-hardening behavior of silty clay gouge, representing a heterogeneous mineral assemblage (Table 1), might therefore actually be caused by the type I artifact. Calcareous ooze gouge, however, is not susceptible to the type I artifact due to its monomict character (Table 1) and indicates a positive dependency of η on effective normal stress. In Figure 8, consecutive effective normal stress steps are identifiable at sharp bends in the layer thickness. Most of the slip-weakening occurrences are recorded in velocity steps showing velocity-strengthening behavior and are therefore not masked
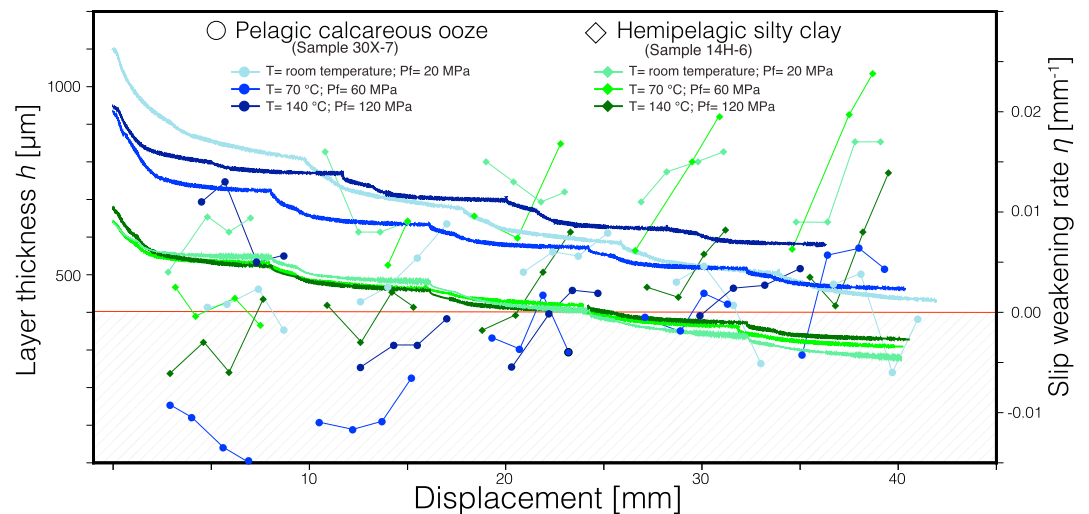
Figure 8. Evolution of experimental gouge layer thickness with displacement (solid lines, left ordinate) and corresponding slip-hardening/weakening rates (symbols, right ordinate) recorded in experiments on pelagic calcareous ooze gouge and hemipelagic silty clay gouge. Color coding refers to the applied experimental conditions and sediment type, respectively. Connected symbols represent respective effective normal stress steps. The red line marks the transition between slip-hardening ($\eta > 0$) and slip-weakening ($\eta < 0$) behavior. Thinning trends are comparable in all experiments except for calcareous ooze gouge at room temperature, which shows considerably stronger thinning. The starting layer thickness, however, strongly differs between calcareous ooze and silty clay gouge, owed to higher compressibility of clays. There is a positive trend in slip-hardening/weakening rate as a function of displacement and effective normal stress.

by the type II artifact. Both materials show differences in η as a function of temperature and pore fluid pressure. This cannot be explained by either experimental artifact.

For the sake of argument, we will assume here that most of the weakening/hardening trends reflect material behavior. Then there is still the issue that these trends are assumed to be steady state and linear. In fact, one could argue that if there is any hardening or weakening, then in actual fact the real slip velocity is different from the load point velocity applied and as such is not steady state and $(a - b)$ is in fact not defined. Moreover, the linear weakening with displacement implies an unrealistically low or even negative friction for the displacements involved in SSE events (e.g., taking η is 0.02 mm^{-1} and a displacement of 10 and 50 mm, gives a friction drop of 0.2 and 0.5, respectively, from a *base* friction of 0.3). The evolution of the microstructure into localized shear bands must at some point be complete as demonstrated, for example, by Logan et al. (1992), so the weakening or hardening must slow down and come to a halt. There are two ways to circumvent the problem of linear weakening: (1) we can define the weakening in terms of strain, rather than displacement or (2) we can treat the weakening as a second state variable. The first approach has a clear physical background. As has been shown by Logan et al. (1992) the development of the microstructure is more a function of shear strain than of absolute displacement: Weakening for gouges with different thicknesses is the same when plotted versus shear strain. The occurrence of accelerating slip can then be thought of being the result of localization, whereas delocalization would result in decelerating slip. The second approach is appealing because it allows us to use the rate-and-state framework to study the nucleation of SSEs, which is then controlled by the relative values of D_{c1} and D_{c2} as well as the relative values of $(a - b_1)$ and $(a - b_2)$. When the second evolution distance is large (on the order of 1 mm), the friction response as seen in laboratory tests with 0.5- to 1-mm displacement would be virtually indistinguishable from a linear response (Figure 9). Fitting these type of data with a second state variable would, however, result in a relative large error in both b_2 and D_{c2}, since not enough data are available. This can only be resolved by allowing more displacement between velocity pertubations, which is beyond the scope of the present manuscript.

At Costa Rica, shallow slow slip is reported to occur within the exceptionally cool temperature range between 12 and 60 °C (Dixon et al., 2014), which differs from the region of major clay dehydration (Saffer & Wallace, 2015). Apart from the discussed reservations, our mechanical data show mildly velocity-strengthening and slip-weakening behavior in this temperature range (Figures 6a and 6e). Subducted carbonates turn out as the most likely candidates for the generation of slow earthquakes via the mechanism proposed by Ikari, Marone,
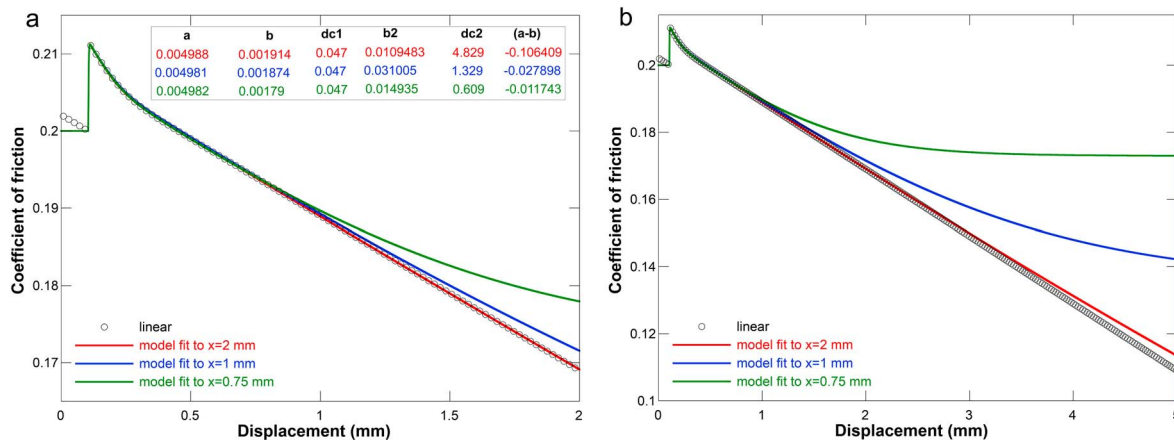
Figure 9. (a, b) Forward calculation of a velocity step of 1 to 10 μm/s with $a = 0.005$, $b = 0.002$, and $dc = 0.05$ mm, plus an additional linear weakening of 0.02 mm^{-1}, along with inversion results of this forward calculation using two state variables and input data to three different amounts of displacement. Rate- and state-dependent friction values from inversion are given in the inset table in (a). The model fit to 0.75 mm gives reasonable values for both $(a − b)$ and d_{c2}, whereas model fits to larger displacements result in unrealistic output values.

et al. (2013). In comparison, the hemipelagic silty clay gouges tend to slip harden and show a strong temperature dependence of η. The frictional behavior to trigger slow slip is given at 140 °C with an approximately 1 order of magnitude higher critical slip-weakening distances (Figures 6b and 6c). Finally, the potential for unstable slow slip increases toward lower effective normal stress. This might explain post seismic slip transients in regions of stress relaxation and negative Coulomb stress transfer. The slip-weakening/hardening data presented by Ikari, Marone, et al. (2013) cover a comparable range ($\approx −0.015 \leq \eta \leq 0.007$). However, their strongly slip-weakening behavior was recorded at room temperature, whereas our samples in the most cases required at least 70 °C for comparably marked values. This discrepancy might be explained by the higher sheet silicate content of Nankai trough clays compared to our silty clays and carbonates.

6.4. Carbonates as Most Likely Candidates for Unstable Slip

The data presented here suggest that the occurrence of differing fault slip modes like the nucleation of large plate boundary earthquakes or SSEs largely depends on the mechanical properties of pelagic sediments from the incoming oceanic plate. Because of the erosive nature of the Costa Rican subduction zone this appears to be surprising, as most of the sediments in the subduction channel should originate from the overriding plate (Vannucchi et al., 2012; von Huene et al., 2004). In our laboratory experiments at conditions corresponding to the updip limit of seismogenesis, only the pelagic calcareous ooze from the incoming plate produced frictional stick-slip instabilities, which have long been considered an analog for natural earthquakes (Brace & Byerlee, 1966). Material that is possibly incorporated into the subduction channel and could not be considered in our experiments is the Osa Mélange, a middle Eocene-middle Miocene rock assemblage dominated by basalt, chert and limestone (Meschede et al., 1999; Vannucchi et al., 2006). In terms of lithology, this assemblage might represent oceanic basalt and its pelagic sedimentary cover.

First results reported from the 2011 3-D seismic survey of the CRISP study area provide important insights into the internal structure of the forearc wedge. The extent of the frontal paleoaccretionary prism reaches presumably 30–40 km landward from the trench (Bangs et al., 2016; Vannucchi et al., 2013, 2017), much more than previously thought. These authors also agree that the bulk of the marginal wedge beneath the middle and upper slope is formed by clastic material. According to Bangs et al. (2016), this clastic material was deposited at about 5 Ma on the incoming plate and was accreted shortly afterward. In addition, the outermost edge of the continental margin represents a small (<10 km wide) but active frontal accretionary prism consisting of pelagic and hemipelagic sediments (Bangs et al., 2016). These findings have far-reaching implications for the material budget within the subduction channel, which is usually compositionally dominated by continental forearc material removed by tectonic erosion. In fact, the first 30–40 km of the forearc consists of previously accreted incoming plate sediments, implying considerable amounts of pelagic and hemipelagic lithologies that may form the base of each consecutive thrust sheet assuming the geometrical model of Vannucchi et al. (2017). Although the relative proportion of such lithologies within the subduction channel is probably low compared to continental clastic sediments, the deformation or fault slip mode along the shallow

part of the megathrust and the updip limit of seismogenesis could be controlled by the mechanical properties of these sediments.

Velocity-weakening (i.e., potentially unstable) behavior of hemipelagic and clastic sediments, preferentially occurring at cold conditions and low effective normal stress representative for the most shallow reaches of the plate boundary, deserves some attention. As already mentioned, the occurrence of frictional instability is controlled by the critical stiffness of the system and is linked to velocity-weakening behavior via equation (7). Here systematical studies investigating the evolution of stiffness as a function of normal stress, temperature, and pore fluid pressure are needed to assess the potential for the emergence of slip instability in such material due to changes in critical stiffness. Alternatively, assuming that stiffness of the testing system (machine + gouge) does not vary seriously among the tests performed with different materials, occurrences of stick slip in calcareous ooze might imply smaller values of D_c. However, it is not possible to verify this, as there are no inversion results (and therefore no D_c values) for instances of stick slip and there is no clear trend in D_c values for our inversion results (supporting information Figure S1). In this context, also the scaling of critical slip distances to natural dimensions needs to be better understood in order to allow for proper quantification of the critical stiffness in nature. At the same time, a microphysical understanding of $(a - b)$ is needed for reliable extrapolation. First steps to realize this have recently been made by Chen and Spiers (2016) and Ikari et al. (2016).

The Costa Rica segment of the MAT is the locus of increased tectonic erosion due to the subduction of the Cocos Ridge. In particular, Cocos Ridge subduction causes a progressive increase in the geothermal gradient toward the ridge axis and results in a shift in seismicity toward shallower levels equivalent to lower normal stresses (Vannucchi et al., 2010). Based on our experiments, this shift of the upper seismognic zone in the vicinity of the Cocos Ridge cannot be explained by the temperature-controlled change in frictional behavior of calcareous ooze gouge alone. Nevertheless, frictional instability of this material does not require any mineral transformations, such as, for example, the smectite to illite transition and is capable of triggering exceptionally shallow seismic events where the geothermal gradient is sufficiently high. Such shallow earthquakes have a high tsunamigenic potential, as related ruptures have a high potential to propagate to the trench. Past slip to the trench at Costa Rica was recently revealed by the discovery of a recent thrust fault cutting the frontal prism at IODP Site U1412 (Vannucchi et al., 2017). In combination with this discovery it was shown that both calcareous oozes and silty clays are approximately equally weak at experimental coseismic slip velocities (cf. Figure 3b of Vannucchi et al., 2017) and can, therefore, host rupture propagation. One of the central messages of Kurzawski et al. (2016), however, is that calcareous oozes are instrumental in nucleating earthquake slip at low, preseismic rates of movement.

7. Summary and Conclusions

We conducted a systematic experimental study on frictional properties of subduction channel input sediments recovered during IODP Expeditions 334 and 344 offshore Costa Rica, covering all major lithologies from the incoming as well as overriding plates. Our main conclusions are as follows:

1. Transitions between different fault slip modes, such as aseismic fault slip, shallow slow earthquakes, and the emergence of plate boundary ruptures, that is, the generation of regular earthquakes at the upper limit of the seismogenic zone, can be explained by the presence of these materials in the subduction channel and their variability in mechanical behavior during progressive subduction.
2. Incoming plate carbonates are the only materials showing unstable slip, which is considered a laboratory analog for regular earthquakes. Hemipelagics show velocity-weakening behavior at low effective normal stress, which might favor rupture propagation toward the trench.
3. The locking degree of the plate boundary fault does not follow the simple assumption of pore pressure related stabilization, as possible direct effects of pore pressure on the velocity dependence of friction are not considered. In our friction experiments, increases in pore fluid pressure generally result in frictional stabilization, except for carbonate gouge, which shows destabilization at $T = 140\,°C$.
4. Linear weakening/hardening trends in RSF data bear a high potential for experimental artifacts and can hardly be assumed as steady state after relatively small amounts of displacement. This, in many cases, would imply unreasonably large drops in friction when transferred to the natural case. Therefore, we argue that the recently proposed mechanism for the emergence of slow earthquakes via slip weakening

(Ikari, Marone, et al., 2013) needs more careful data evaluation. Nevertheless, our data show systematic variations in slip-weakening/hardening rates with implications for slip mode transition in subduction channels, if the mechanism can be approved. Slip weakening appears to be thermally activated in all materials tested but requires higher or lower temperatures dependent on sediment type. Incoming plate carbonates consistently show slip-weakening behavior at $T = 70\,°C$ and in cases already at room temperature. Therefore, they are considered the most likely candidates to trigger shallow slow earthquakes, which in Costa Rica are reported to occur within the exceptionally cool temperature range between 12 and 60 °C (Dixon et al., 2014).

We propose that shallow subduction channel deformation, that is, from trench to updip limit of seismogenesis within the erosive subduction system at Costa Rica, is governed by the mechanical behavior of the material conveyed with the incoming plate. This is in accordance to the new findings that the forearc is built up by previously accreted sediments. A paleoaccretionary wedge characterized by fault propagation folds reaches presumably 30–40 km landward from the trench, whereas the first ≈5 km is actually formed by an embryonic active frontal accretionary prism (Bangs et al., 2016; Vannucchi et al., 2017). The margin evolution is characterized by transient phases of accretion and nonaccretion/tectonic erosion. This means that the subduction channel influx from the incoming Cocos Plate is significant and plays an important role in deformation processes.

References

Arroyo, I. G., Grevemeyer, I., Ranero, C. R., & Von Huene, R. (2014). Interplate seismicity at the CRISP drilling site: The 2002 Mw 6.4 Osa Earthquake at the southeastern end of the Middle America Trench. *Geochemistry, Geophysics, Geosystems*, *15*, 3,035–3,050. https://doi.org/10.1002/2014GC005359

Arroyo, I. G., Grevemeyer, I., Von Huene, R., Husen, S., Ranero, C. R., & Behrmann, J. (2011). Interplate seismicity at the CRISP site: The 2002 Osa earthquake sequence. *AGU Fall Meeting Abstracts*, *1*, 2,348.

Bangs, N. L., McIntosh, K. D., Silver, E. A., Kluesner, J. W., & Ranero, C. R. (2016). A recent phase of accretion along the southern Costa Rican subduction zone. *Earth and Planetary Science Letters*, *443*, 204–215.

Bangs, N. L., McIntosh, K. D., Silver, E. A., Kluesner, J. W., & Ranero, C. R. (2015). Fluid accumulation along the Costa Rica subduction thrust and development of the seismogenic zone. *Journal of Geophysical Research: Solid Earth*, *120*, 67–86. https://doi.org/10.1002/2014JB011265

Barckhausen, U., Ranero, C. R., Huene, R. v., Cande, S. C., & Roeser, H. A. (2001). Revised tectonic boundaries in the Cocos Plate off Costa Rica: Implications for the segmentation of the convergent margin and for plate tectonic models. *Journal of Geophysical Research*, *106*(B9), 19,207–19,220.

Beeler, N., Tullis, T., & Weeks, J. (1994). The roles of time and displacement in the evolution effect in rock friction. *Geophysical Research Letters*, *21*(18), 1,987–1,990.

Bekins, B. A., & Dreiss, S. J. (1992). A simplified analysis of parameters controlling dewatering in accretionary prisms. *Earth and Planetary Science Letters*, *109*(3), 275–287.

Bilek, S. L., Schwartz, S. Y., & DeShon, H. R. (2003). Control of seafloor roughness on earthquake rupture behavior. *Geology*, *31*(5), 455–458.

Blanpied, M. L., Tullis, T. E., & Weeks, J. D. (1998). Effects of slip, slip rate, and shear heating on the friction of granite. *Journal of Geophysical Research*, *103*(B1), 489–511.

Brace, W., & Byerlee, J. (1966). Stick-slip as a mechanism for earthquakes. *Science*, *153*(3739), 990–992.

Bray, C., & Karig, D. (1985). Porosity of sediments in accretionary prisms and some implications for dewatering processes. *Journal of Geophysical Research*, *90*(B1), 768–778.

Byrne, D. E., Davis, D. M., & Sykes, L. R. (1988). Loci and maximum size of thrust earthquakes and the mechanics of the shallow region of subduction zones. *Tectonics*, *7*(4), 833–857.

Carpenter, B., Ikari, M., & Marone, C. (2016). Laboratory observations of time-dependent frictional strengthening and stress relaxation in natural and synthetic fault gouges. *Journal of Geophysical Research: Solid Earth*, *121*, 1,183–1,201. https://doi.org/10.1002/2015JB012136

Carpenter, B., Scuderi, M., Collettini, C., & Marone, C. (2014). Frictional heterogeneities on carbonate-bearing normal faults: Insights from the Monte Maggio Fault, Italy. *Journal of Geophysical Research: Solid Earth*, *119*, 9,062–9,076. https://doi.org/10.1002/2014JB011337

Chen, J., & Spiers, C. J. (2016). Rate and state frictional and healing behavior of carbonate fault gouge explained using microphysical model. *Journal of Geophysical Research: Solid Earth*, *121*, 8,642–8,665. https://doi.org/10.1002/2016JB013470

Chen, J., Verberne, B. A., & Spiers, C. J. (2015). Interseismic re-strengthening and stabilization of carbonate faults by "non-Dieterich" healing under hydrothermal conditions. *Earth and Planetary Science Letters*, *423*, 1–12.

Clayton, C., Müller Steinhagen, H., & Powrie, W. (1995). Terzaghi's theory of consolidation, and the discovery of effective stress. *Inproceedings of the Institution of Civil Engineers: Geotechnical Engineering*, *113*(4), 191–205.

Clift, P., & Vannucchi, P. (2004). Controls on tectonic accretion versus erosion in subduction zones: Implications for the origin and recycling of the continental crust. *Reviews of Geophysics*, *42*, RG2001. https://doi.org/10.1029/2003RG000127

Coulomb, C. (1776). Sur une application des règles maximis et minimis a quelques problèmes de statique, relatives à l'architecture. *Académie des Sciences Paris, Memorial Mathé,matiques et Physique*, *7*, 343–382.

DeMaster, D. J. (1981). The supply and accumulation of silica in the marine environment. *Geochimica et Cosmochimica Acta*, *45*(10), 1,715–1,732.

DeMets, C. (2001). A new estimate for present-day Cocos-Caribbean plate motion: Implications for slip along the Central American volcanic arc. *Geophysical Research Letters*, *28*(21), 4,043–4,046.

DeShon, H. R., Schwartz, S. Y., Bilek, S. L., Dorman, L., Gonzalez, V., Protti, J., et al. (2003). Seismogenic zone structure of the southern Middle America Trench, Costa Rica. *Journal of Geophysical Research*, *108*(B10), 2491. https://doi.org/10.1029/2002JB002294

Den Hartog, S., Niemeijer, A., & Spiers, C. (2012). New constraints on megathrust slip stability under subduction zone P-T conditions. *Earth and Planetary Science Letters*, *353*, 240–252.

Den Hartog, S. A., Peach, C. J., de Winter, D. M., Spiers, C. J., & Shimamoto, T. (2012). Frictional properties of megathrust fault gouges at low sliding velocities: New data on effects of normal stress and temperature. *Journal of Structural Geology*, *38*, 156–171.

Dieterich, J. H. (1972). Time-dependent friction in rocks. *Journal of Geophysical Research*, *77*(20), 3,690–3,697.

Dieterich, J. H. (1979). Modeling of rock friction: 1. Experimental results and constitutive equations. *Journal of Geophysical Research*, *84*(B5), 2,161–2,168.

Dinc, A. N., Koulakov, I., Thorwart, M., Rabbel, W., Flueh, E. R., Arroyo, I., et al. (2010). Local earthquake tomography of central Costa Rica: transition from seamount to ridge subduction. *Geophysical Journal International*, *183*(1), 286–302.

Dixon, T. H., Jiang, Y., Malservisi, R., McCaffrey, R., Voss, N., Protti, M., & Gonzalez, V. (2014). Earthquake and tsunami forecasts: Relation of slow slip events to subsequent earthquake rupture. *Proceedings of the National Academy of Sciences*, *111*(48), 17,039–17,044.

Expedition 334 Scientists (2012a). Site U1378. In *Proceedings of the Integrated Ocean Drilling Program*, Integrated Ocean Drilling Program Management International, Inc., Tokyo. vol. 334 https://doi.org/10.2204/iodp.proc.334.103.2012

Expedition 334 Scientists (2012b). Site U1379. In *Proceedings of the Integrated Ocean Drilling Program*, Integrated Ocean Drilling Program Management International, Inc., Tokyo. vol. 334 https://doi.org/10.2204/iodp.proc.334.104.2012

Harris, R., Sakaguchi, A., Petronotis, K., Baxter, A., Berg, R., Burkett, A., et al. (2013a). Input Site U1414. In *Proceedings of the Integrated Ocean Drilling Program*, Integrated Ocean Drilling Program, College Station, TX. vol. 344 https://doi.org/10.2204/iodp.proc.344.104.2013

Harris, R., Sakaguchi, A., Petronotis, K., Baxter, A., Berg, R., Burkett, A., et al. (2013b). Frontal prism Site U1412. In *Proceedings of the Integrated Ocean Drilling Program*, Integrated Ocean Drilling Program, College Station, TX. vol. 344 https://doi.org/10.2204/iodp.proc.344.105.2013

Husen, S., Kissling, E., & Quintero, R. (2002). Tomographic evidence for a subducted seamount beneath the Gulf of Nicoya, Costa Rica: The cause of the 1990 M_w = 7.0 Gulf of Nicoya earthquake. *Geophysical Research Letters*, *29*(8), 1238. https://doi.org/10.1029/2001GL014045

Hyndman, R., & Wang, K. (1993). Thermal constraints on the zone of major thrust earthquake failure: The Cascadia subduction zone. *Journal of Geophysical Research*, *98*(B2), 2,039–2,060.

Hyndman, R., Yamano, M., & Oleskevich, D. (1997). The seismogenic zone of subduction thrust faults. *Island Arc*, *6*(3), 244–260.

Ikari, M. J., Carpenter, B. M., & Marone, C. (2016). A microphysical interpretation of rate- and state-dependent friction for fault gouge. *Geochemistry, Geophysics, Geosystems*, *17*, 1,660–1,677. https://doi.org/10.1002/2016GC006286

Ikari, M. J., Marone, C., Saffer, D. M., & Kopf, A. J. (2013). Slip weakening as a mechanism for slow earthquakes. *Nature Geoscience*, *6*(6), 468–472.

Ikari, M. J., Niemeijer, A. R., Spiers, C. J., Kopf, A. J., & Saffer, D. M. (2013). Experimental evidence linking slip instability with seafloor lithology and topography at the Costa Rica convergent margin. *Geology*, *41*(8), 891–894.

Jiang, Y., Wdowinski, S., Dixon, T. H., Hackl, M., Protti, M., & Gonzalez, V. (2012). Slow slip events in Costa Rica detected by continuous GPS observations, 2002–2011. *Geochemistry, Geophysics, Geosystems*, *13*, Q04006. https://doi.org/10.1029/2012GC004058

Kameda, J., Harris, R. N., Shimizu, M., Ujiie, K., Tsutsumi, A., Ikehara, M., et al. (2015). Hydrogeological responses to incoming materials at the erosional subduction margin, offshore Osa Peninsula, Costa Rica. *Geochemistry, Geophysics, Geosystems*, *16*, 2,725–2,742. https://doi.org/10.1002/2015GC005837

Kastner, W., Roehrich, E., Schmitt, W., & Steinbuch, R. (1981). Critical crack sizes in ductile piping. *International Journal of Pressure Vessels and Piping*, *9*(3), 197–219.

Kopf, A. (2013). Effective strength of incoming sediments and its implications for plate boundary propagation: Nankai and Costa Rica as type examples of accreting vs. erosive convergent margins. *Tectonophysics*, *608*, 958–969.

Kurzawski, R. M., Stipp, M., Niemeijer, A. R., Spiers, C. J., & Behrmann, J. H. (2016). Earthquake nucleation in weak subducted carbonates. *Nature Geoscience*, *9*(9), 717.

LaFemina, P., Dixon, T. H., Govers, R., Norabuena, E., Turner, H., Saballos, A., et al. (2009). Fore-arc motion and Cocos Ridge collision in Central America. *Geochemistry, Geophysics, Geosystems*, *10*, Q05S14. https://doi.org/10.1029/2008GC002181

Logan, J., Dengo, C., Higgs, N., & Wang, Z. (1992). Fabrics of experimental fault zones: Their development and relationship to mechanical behavior. *International Geophysics*, *51*, 33–67.

Logan, J. M., & Rauenzahn, K. A. (1987). Frictional dependence of gouge mixtures of quartz and montmorillonite on velocity, composition and fabric. *Tectonophysics*, *144*(1–3), 87–108.

Lücke, O. H., & Arroyo, I. G. (2015). Density structure and geometry of the Costa Rican subduction zone from 3-D gravity modeling and local earthquake data. *Solid Earth*, *6*(4), 1,169–1,183.

Lupini, J., Skinner, A., & Vaughan, P. (1981). The drained residual strength of cohesive soils. *Geotechnique*, *31*(2), 181–213.

Marone, C. (1998a). Laboratory-derived friction laws and their application to seismic faulting. *Annual Review of Earth and Planetary Sciences*, *26*(1), 643–696.

Marone, C. (1998b). The effect of loading rate on static friction and the rate of fault healing during the earthquake cycle. *Nature*, *391*(6662), 69–72.

Marone, C., & Saffer, D. (2015). The mechanics of frictional healing and slip instability during the seismic cycle. *Treatise on Geophysics*, *4*, 111–138.

Meschede, M., Zweigel, P., Frisch, W., & Volker, D. (1999). Mélange formation by subduction erosion: The case of the Osa mélange in southern Costa Rica. *Terra Nova-Oxford*, *11*(4), 141–148.

Mitchell, J. K., & Soga, K. (2005). *Fundamentals of Soil Behavior*. Hoboken, N.J.: Wiley.

Mohr, O. (1900). Welche Umstände bedingen die Elastizitätsgrenze und den Bruch eines Materials. *Zeitschrift des Vereins Deutscher Ingenieure*, *46*(1524-1530), 1,572–1,577.

Morrow, C., Moore, D. E., & Lockner, D. (2000). The effect of mineral bond strength and adsorbed water on fault gouge frictional strength. *Geophysical Research Letters*, *27*(6), 815–818.

Morrow, C., Radney, B., & Byerlee, J. (1992). Frictional strength and the effective pressure law of montmorillonite and illite clays. *International Geophysics*, *51*, 69–88.

Morrow, C., Shi, L., & Byerlee, J. (1982). Strain hardening and strength of clay-rich fault gouges. *Journal of Geophysical Research*, *87*(B8), 6,771–6,780.

Müller, P. J., & Schneider, R. (1993). An automated leaching method for the determination of opal in sediments and particulate matter. *Deep Sea Research Part I: Oceanographic Research Papers*, *40*(3), 425–444.

Neuzil, C. (1995). Abnormal pressures as hydrodynamic phenomena. *American Journal of Science*, *295*(6), 742.

Newman, A. V., Schwartz, S. Y., Gonzalez, V., DeShon, H. R., Protti, J., & Dorman, L. M. (2002). Along-strike variability in the seismogenic zone below Nicoya Peninsula, Costa Rica. *Geophysical Research Letters*, *29*(20), 1977. https://doi.org/10.1029/2002GL015409

Niemeijer, A., Spiers, C., & Peach, C. (2008). Frictional behaviour of simulated quartz fault gouges under hydrothermal conditions: Results from ultra-high strain rotary shear experiments. *Tectonophysics*, *460*(1), 288–303.

Oleskevich, D., Hyndman, R., & Wang, K. (1999). The updip and downdip limits to great subduction earthquakes: Thermal and structural models of Cascadia, south Alaska, SW Japan, and Chile. *Journal of Geophysical Research*, *104*(B7), 14,965–14,991.

Protti, M., Gïendel, F., & McNally, K. (1995). Correlation between the age of the subducting Cocos Plate and the geometry of the Wadati-Benioff zone under Nicaragua and Costa Rica. *Geological Society of America Special Papers*, *295*, 309–326.

Protti, M., Gu, F., & McNally, K. (1994). The geometry of the Wadati-Benioff zone under southern Central America and its tectonic significance: Results from a high-resolution local seismographic network. *Physics of the Earth and Planetary Interiors*, *84*(1–4), 271–287.

Pytte, A. M., & Reynolds, R. C. (1989). The thermal transformation of smectite to illite. In *Thermal history of sedimentary basins* (pp. 133–140). New York, NY: Springer.

Ranero, C. R., Grevemeyer, I., Sahling, H., Barckhausen, U., Hensen, C., Wallmann, K., et al. (2008). Hydrogeological system of erosional convergent margins and its influence on tectonics and interplate seismogenesis. *Geochemistry, Geophysics, Geosystems*, *9*, Q03S04. https://doi.org/10.1029/2007GC001679

Ranero, C. R., Huene, R., Flueh, E., Duarte, M., Baca, D., & McIntosh, K. (2000). A cross section of the convergent Pacific margin of Nicaragua. *Tectonics*, *19*(2), 335–357.

Ranero, C. R., & von Huene, R. (2000). Subduction erosion along the Middle America convergent margin. *Nature*, *404*(6779), 748–752.

Reinen, L. A., & Weeks, J. D. (1993). Determination of rock friction constitutive parameters using an iterative least squares inversion method. *Journal of Geophysical Research*, *98*(B9), 15,937–15,950.

Ruina, A. (1983). Slip instability and state variable friction laws. *Journal of Geophysical Research*, *88*(B12), 10,359–10,370.

Saffer, D. M., & Bekins, B. A. (2006). An evaluation of factors influencing pore pressure in accretionary complexes: Implications for taper angle and wedge mechanics. *Journal of Geophysical Research*, *111*, B04101. https://doi.org/10.1029/2005JB003990

Saffer, D. M., Frye, K. M., Marone, C., & Mair, K. (2001). Laboratory results indicating complex and potentially unstable frictional behavior of smectite clay. *Geophysical Research Letters*, *28*(12), 2,297–2,300.

Saffer, D. M., Lockner, D. A., & McKiernan, A. (2012). Effects of smectite to illite transformation on the frictional strength and sliding stability of intact marine mudstones. *Geophysical Research Letters*, *39*, L11304. https://doi.org/10.1029/2012GL051761

Saffer, D. M., & Marone, C. (2003). Comparison of smectite-and illite-rich gouge frictional properties: Application to the updip limit of the seismogenic zone along subduction megathrusts. *Earth and Planetary Science Letters*, *215*(1), 219–235.

Saffer, D. M., & Tobin, H. J. (2011). Hydrogeology and mechanics of subduction zone forearcs: Fluid flow and pore pressure. *Annual Review of Earth and Planetary Sciences*, *39*, 157–186.

Saffer, D. M., & Wallace, L. M. (2015). The frictional, hydrologic, metamorphic and thermal habitat of shallow slow earthquakes. *Nature Geoscience*, *8*(8), 594–600. https://doi.org/10.1038/ngeo2490

Schlüter, M., & Rickert, D. (1998). Effect of pH on the measurement of biogenic silica. *Marine Chemistry*, *63*(1), 81–92.

Scholz, C. H. (1998). Earthquakes and friction laws. *Nature*, *391*(6662), 37–42.

Shimamoto, T., Seno, T., & Uyeda, S. (1993). A simple rheological framework for comparative subductology. *Relating Geophysical Structures and Process: The Jeffreys Volume: Geophys. Monogr. Ser*, *76*, 39–52.

Spagnuolo, E., Plümper, O., Violay, M., Cavallo, A., & Di Toro, G. (2015). Fast-moving dislocations trigger flash weakening in carbonate-bearing faults during earthquakes. *Scientific Reports*, *5*, 16112.

Spinelli, G. A., Saffer, D. M., & Underwood, M. B. (2006). Hydrogeologic responses to three-dimensional temperature variability, Costa Rica subduction margin. *Journal of Geophysical Research*, *111*, B04403. https://doi.org/10.1029/2004JB003436

Spinelli, G. A., & Underwood, M. B. (2004). Character of sediments entering the Costa Rica subduction zone: Implications for partitioning of water along the plate interface. *Island Arc*, *13*(3), 432–451.

Terzaghi, K. v. (1923). Die Berechnung der Durchlassigkeitsziffer des Tones aus dem Verlauf der hydrodynamischen Spannungserscheinungen. *Sitzungsberichte der Akademie der Wissenschaften in Wien, Mathematisch-Naturwissenschaftliche Klasse, Abteilung IIa*, *132*, 125–138.

Tesei, T., Collettini, C., Barchi, M. R., Carpenter, B. M., & Di Stefano, G. (2014). Heterogeneous strength and fault zone complexity of carbonate-bearing thrusts with possible implications for seismicity. *Earth and Planetary Science Letters*, *408*, 307–318.

Tesei, T., Collettini, C., Viti, C., & Barchi, M. R. (2013). Fault architecture and deformation mechanisms in exhumed analogues of seismogenic carbonate-bearing thrusts. *Journal of Structural Geology*, *55* 167–181.

Vannucchi, P., Fisher, D. M., Bier, S., & Gardner, T. W. (2006). From seamount accretion to tectonic erosion: Formation of Osa Mélange and the effects of Cocos Ridge subduction in southern Costa Rica. *Tectonics*, *25*, TC2004. https://doi.org/10.1029/2006TC002013

Vannucchi, P., Morgan, J. P., Silver, E. A., & Kluesner, J. W. (2016). Origin and dynamics of depositionary subduction margins, *Geochemistry, Geophysics, Geosystems*, *17*, 1,966–1,974. https://doi.org/10.1002/2016GC006259

Vannucchi, P., Ranero, C. R., Galeotti, S., Straub, S. M., Scholl, D. W., & McDougall-Ried, K. (2003). Fast rates of subduction erosion along the Costa Rica Pacific margin: Implications for nonsteady rates of crustal recycling at subduction zones. *Journal of Geophysical Research*, *108*(B11), 2511. https://doi.org/10.1029/2002JB002207

Vannucchi, P., Sage, F., Phipps Morgan, J., Remitti, F., & Collot, J.-Y. (2012). Toward a dynamic concept of the subduction channel at erosive convergent margins with implications for interplate material transfer. *Geochemistry, Geophysics, Geosystems*, *13*, Q02003. https://doi.org/10.1029/2011GC003846

Vannucchi, P., Sak, P. B., Morgan, J. P., Ohkushi, K., & Ujiie, K. (2013). Rapid pulses of uplift, subsidence, and subduction erosion offshore Central America: Implications for building the rock record of convergent margins. *Geology*, *41*(9), 995–998.

Vannucchi, P., Scholl, D. W., Meschede, M., & McDougall-Reid, K. (2001). Tectonic erosion and consequent collapse of the Pacific margin of Costa Rica: Combined implications from ODP Leg 170, seismic offshore data, and regional geology of the Nicoya Peninsula. *Tectonics*, *20*(5), 649–668.

Vannucchi, P., Spagnuolo, E., Aretusini, S., Di Toro, G., Ujiie, K., Tsutsumi, A., & Nielsen, S. (2017). Past seismic slip-to-the-trench recorded in Central America megathrust. *Nature Geoscience*, *10*(12), 935–940.

Vannucchi, P., Ujiie, K., & Gamage, K. (2010). Costa Rica Seismogenesis Project (CRISP): Sampling and quantifying input to the seismogenic zone and fluid output. *IODP Scientific Prospectus*, *334*.

Verberne, B. A., de Bresser, J. H., Niemeijer, A. R., Spiers, C. J., de Winter, D. M., & Plümper, O. (2013). Nanocrystalline slip zones in calcite fault gouge show intense crystallographic preferred orientation: Crystal plasticity at sub-seismic slip rates at 18–150 °C. *Geology*, *41*(8), 863–866.

Verberne, B. A., Plümper, O., de Winter, D. M., & Spiers, C. J. (2014). Superplastic nanofibrous slip zones control seismogenic fault friction. *Science*, *346*(6215), 1,342–1,344.

Verberne, B., Spiers, C., Niemeijer, A., De Bresser, J., De Winter, D., & Plümper, O. (2014). Frictional properties and microstructure of calcite-rich fault gouges sheared at sub-seismic sliding velocities. *Pure and Applied Geophysics*, *171*(10), 2,617–2,640.

von Huene, R., Ranero, C. R., & Vannucchi, P. (2004). Generic model of subduction erosion. *Geology*, *32*(10), 913–916.

von Huene, R. V., Ranero, C. R., Weinrebe, W., & Hinz, K. (2000). Quaternary convergent margin tectonics of Costa Rica, segmentation of the Cocos Plate, and Central American volcanism. *Tectonics*, *19*(2), 314–334.

Walther, C. H. (2003). The crustal structure of the Cocos ridge off Costa Rica. *Journal of Geophysical Research*, *108*(B3), 2136. https://doi.org/10.1029/2001JB000888

Wojdyr, M. (2010). Fityk: A general-purpose peak fitting program. *Journal of Applied Crystallography*, *43*(5–1), 1,126–1,128.